

1 **Influence of Shear Heating and Thermomechanical**  
2 **Coupling on Earthquake Sequences and the**  
3 **Brittle-Ductile Transition**

4 **Kali L. Allison<sup>1,2</sup>, Eric M. Dunham<sup>1,3</sup>**

5 <sup>1</sup>Department of Geophysics, Stanford University, Stanford, California, USA

6 <sup>2</sup>now at: Department of Geology, University of Maryland, College Park, Maryland, USA

7 <sup>3</sup>Institute for Computational and Mathematical Engineering, Stanford University, Stanford, California,  
8 USA

9 **Key Points:**

- 10 • Earthquake modeling predicts viscous shear zones a few kilometers wide below faults  
11 • Shear heating creates a thermal anomaly of tens to hundreds of degrees in the lower  
12 crust  
13 • Shear heating raises the brittle-ductile transition and can limit rupture depth

## Abstract

Localized frictional sliding on faults in the continental crust transitions at depth to distributed deformation in viscous shear zones. This brittle-ductile transition (BDT), and/or the transition from velocity-weakening (VW) to velocity-strengthening (VS) friction, are controlled by the lithospheric thermal structure and composition. Here we investigate these transitions, and their effect on the depth extent of earthquakes, using 2D antiplane shear simulations of a strike-slip fault with rate-and-state friction. The off-fault material is viscoelastic, with temperature-dependent dislocation creep. We solve the heat equation for temperature, accounting for frictional and viscous shear heating that creates a thermal anomaly relative to the ambient geotherm which reduces viscosity and facilitates viscous flow. We explore several geotherms and effective normal stress distributions (by changing pore pressure), quantifying the thermal anomaly, seismic and aseismic slip, and the transition from frictional sliding to viscous flow. The thermal anomaly can reach several hundred degrees below the seismogenic zone in models with hydrostatic pressure, but is smaller for higher pressure (and these high-pressure models are most consistent with San Andreas Fault heat flow constraints). Shear heating raises the BDT, sometimes to where it limits rupture depth rather than the frictional VW-to-VS transition. Our thermomechanical modeling framework can be used to evaluate lithospheric rheology and thermal models through predictions of earthquake ruptures, postseismic and interseismic crustal deformation, heat flow, and the geological structures that reflect the complex deformation beneath faults.

## 1 Introduction

Thermal structure plays a major role in the rheology and dynamics of the continental lithosphere and active faults embedded within it. Increasing temperature with depth activates crystal-plastic creep, also called viscous flow, producing the well-known transition from localized frictional sliding across faults (i.e., brittle deformation) to viscous flow (i.e., ductile deformation) (e.g., Byerlee, 1978; Goetze & Evans, 1979; Brace & Kohlstedt, 1980; Sibson, 1982, 1984). Below the brittle-ductile transition (BDT), crystal-plastic creep reduces the flow stress of lithospheric rocks, preventing seismic slip and producing a zone of viscous deformation that forms the ductile root of faults. Temperature also influences the frictional properties of faults, with many experiments providing evidence for a transition from steady-state velocity-weakening to velocity-strengthening friction as temperature is increased, as reviewed by Hu & Sun (2020). Experiments suggest that granite and related crustal rocks undergo this transition at roughly 350 °C (e.g., Dieterich, 1978; Ruina, 1983; Tullis & Weeks, 1986; Blanpied et al., 1991, 1995; Chester, 1995; Aharonov & Scholz, 2018, 2019), though other experiments suggest that these rocks can remain velocity-weakening up to 600 °C (Mitchell et al., 2016). The velocity-weakening portion of a fault can host earthquakes, while velocity-strengthening portions generally slip aseismically. Both the brittle-ductile transition and the frictional stability transition have the potential to affect the extent of the seismogenic zone and the depth to which large ruptures will propagate. Furthermore, due to the temperature-dependence of viscous flow, the depth of the BDT can be altered by frictional and viscous shear heating, which produces a thermal anomaly (i.e., temperature deviation from the ambient geotherm) within and around fault zones. A variety of observations, on both active and exhumed faults, provide insight into the extent of the heat generation and its effect on the structure and dynamics of faults and their roots.

Field observations of exhumed seismogenic zones of faults reveal that, while the overall fault zone in the upper crust may be hundreds of meters wide, slip during individual earthquakes might be localized onto narrow zones that are just tens of microns to centimeters wide (e.g., Chester & Chester, 1998; Wibberley & Shimamoto, 2002; Sibson, 2003; Chester et al., 2004; Noda & Shimamoto, 2005; Rice, 2006). As temperature increases with depth, this highly localized, brittle deformation style ultimately transi-

66 tions into more distributed viscous deformation in the form of relatively broad mylonite  
67 zones. Seismic imaging and seismicity studies of active faults, as well as geologic stud-  
68 ies of exhumed fault zones, reveal a rich array of deformation styles and degree of local-  
69 ization in the middle and lower crust and upper mantle. Many continental transform faults  
70 persist as highly localized features to the Moho or even below it, such as the San An-  
71 dreas and San Jacinto Faults (Lemiszki & Brown, 1988; Henstock et al., 1997; Zhu, 2000;  
72 Vauchez & Tommasi, 2003; Lekic et al., 2011; Miller et al., 2014) and the Newport-Inglewood  
73 Fault (Inbal et al., 2016). Others, including the Dead Sea, Alpine, and Wairau Faults,  
74 apparently transition into distributed zones of deformation in the lower crust (Klosko  
75 et al., 1999; Molnar, 1999; Weber et al., 2004). Some major exhumed mylonite zones from  
76 the lower crust, such as the Great Slave Lake shear zone, the South American shear zone,  
77 and the Woodroffe Thrust mylonite zone (Bell, 1978; Berthe et al., 1979; Weijermars,  
78 1987; Camacho et al., 1995; Hanmer, 1988), can be tens of kilometers in width. How-  
79 ever, because the upper crustal fault zone has eroded away, it is not clear if these zones  
80 are the result of a single fault broadening into a shear zone, or the lower crustal signa-  
81 ture of a zone of anastomosing faults in the brittle crust above (Norris & Cooper, 2003).  
82 Other exhumed mylonite zones are relatively narrow, such as the 1 to 2-km-wide my-  
83 lonite zone from the middle and lower crust beneath the Alpine Fault (Norris & Cooper,  
84 2003; Norris & Toy, 2014) and the 2-km-wide mylonite zone in the Salzach–Ennstal–Mariazell–Puchberg  
85 Fault system (Rosenberg & Schneider, 2008; Frost et al., 2011). Some exhumed fault zones  
86 have features such as mutually overprinted pseudotachylite and mylonite that are in-  
87 terpreted as evidence for rupture propagation below the BDT (e.g., Vissers et al., 1997;  
88 Sibson & Toy, 2006; Lin et al., 2005; Cole et al., 2007; Griffith et al., 2008; Frost et al.,  
89 2011; White, 2012; Kirkpatrick & Rowe, 2013; Melosh et al., 2018; Petley-Ragan et al.,  
90 2019).

91 These transitions in deformation style with depth are also reflected in the strength  
92 profiles of the lithosphere. The lithosphere is typically divided into three layers: the up-  
93 per crust, lower crust, and upper mantle. The upper crust is brittle, so its strength is  
94 determined by the frictional strength of faults. The transition to viscous flow generally  
95 occurs in the lower crust or upper mantle, with their strength depending on their com-  
96 position, water content and presence of partial melt, and the strain rate of deformation.  
97 The continental lithosphere near transform faults may be best described by the “*crème*  
98 *brûlée*” model, in which the upper mantle is weaker than the lower crust (e.g., Maggi  
99 et al., 2000; Jackson, 2002; Bürgmann & Dresen, 2008). This model is supported, in re-  
100 gions such as the Mojave Desert in southern California, by estimates of the rheological  
101 structure from exhumed xenoliths and transient postseismic deformation (e.g., Johnson  
102 et al., 2007; Thatcher & Pollitz, 2008; Behr & Hirth, 2014; Behr & Platt, 2014; Chatzaras  
103 et al., 2015). Other observations also support this view of a weak upper mantle. Behr  
104 & Platt (2014) created a global compilation of shear stress measurements from exhumed  
105 large-scale ductile shear zones and active faults, and found that the middle crust at and  
106 below the BDT is the main load-bearing layer in the lithosphere. They also found that  
107 the brittle upper crust was relatively weak. Many of their lowest estimates for fault strength  
108 come from mature faults such as the San Andreas and Denali Faults, indicating that ma-  
109 ture faults may be weak (Behr & Platt, 2014). It may be that the continental lithosphere  
110 cannot be reduced to a simple layered model like the “*crème brûlée*” model, and that  
111 lateral variations in rheology must be accounted for (e.g., Bürgmann & Dresen, 2008;  
112 Jackson et al., 2008; Wright et al., 2013). In particular, the strength of the crust and man-  
113 tle may be significantly reduced in the vicinity of major faults as a result of weakening  
114 mechanisms such as shear heating and grain-size reduction, and as a result one must take  
115 care in interpreting postseismic deformation (Bürgmann & Dresen, 2008; Wright et al.,  
116 2013).

117 One avenue of research that synthesizes many of these observations is the simula-  
118 tion of sequences of earthquake and aseismic slip, in which the coseismic, postseismic,  
119 and interseismic phases of the earthquake cycle are modeled within a single simulation

120 framework. Many such studies have focused on faults with rate-and-state friction in lin-  
 121 ear elastic half-spaces (e.g., Tse & Rice, 1986; Rice, 1993; Lapusta et al., 2000; Kaneko  
 122 et al., 2011; Erickson & Dunham, 2014). These models can be calibrated to match cose-  
 123 seismic, postseismic, and interseismic observations (Barbot et al., 2012). Other earth-  
 124 quake cycle studies have utilized viscoelastic bulk rheologies but with kinematically im-  
 125 posed earthquakes (e.g., Savage & Prescott, 1978; Thatcher, 1983; Thatcher & England,  
 126 1998; Johnson et al., 2007; Takeuchi & Fialko, 2012; Zhang & Sagiya, 2017). A few mod-  
 127 els fully couple rate-and-state friction and a linear or power-law viscoelastic bulk rhe-  
 128 ology. Some consider a fault-containing elastic layer over a viscoelastic half-space (Kato,  
 129 2002; Lambert & Barbot, 2016a). Others simulate only a single event rather than mul-  
 130 tiple cycles (Barbot & Fialko, 2010; Aagaard et al., 2013). An alternative approach was  
 131 taken by Shimamoto & Noda (2014) and Beeler et al. (2018), who captured the frictional  
 132 sliding to viscous flow transition through a unified constitutive law applied on an “in-  
 133 terface” in an otherwise elastic solid. This approach is based on the assumption that vis-  
 134 cuous flow is confined to a ductile fault root whose width (which must be specified a pri-  
 135 ori) is far less other length scales of interest. Most recently, in Allison & Dunham (2018),  
 136 we developed a method for simulating earthquake sequences on a rate-and-state frictional  
 137 fault embedded within a viscoelastic solid. The transition from fault slip to viscous flow,  
 138 and the width of the fault root, are determined as part of the solution, and can vary spa-  
 139 tially and temporally, unlike the methods reviewed above. Miyake & Noda (2019) have  
 140 also coupled rate-and-state friction with bulk viscoelasticity, exploring how viscous stress  
 141 relaxation can alter or suppress slip as the Maxwell time approaches or becomes smaller  
 142 than the earthquake recurrence interval. However, their spectral boundary integral equa-  
 143 tion method is limited to homogeneous, linear viscoelastic solids, so cannot capture the  
 144 depth-dependent transitions that comprise the focus of Allison & Dunham (2018) and  
 145 our current study.

146 A few studies have considered frictional and viscous shear heating, and the asso-  
 147 ciated thermal anomaly, in the context of earthquake cycles. Models which include only  
 148 viscous shear heating, and use the geometry of a fault-containing layer over a viscoelas-  
 149 tic half-space, provide the following estimates of thermal anomaly: 1-20 °C (Lyzenga et  
 150 al., 1991; Savage & Lachenbruch, 2003) or up to a few hundred °C (Thatcher & Eng-  
 151 land, 1998; Leloup et al., 1999; Takeuchi & Fialko, 2012; Moore & Parsons, 2015). We  
 152 note that Lyzenga et al. (1991) use a weak viscous rheology that places the BDT at only  
 153 7 km depth (for a high stress fault model and power-law flow, similar to our model) and  
 154 reduces shear heating by about an order of magnitude, relative to other studies, at a given  
 155 stress level. The low thermal anomaly estimate of Savage & Lachenbruch (2003) stems  
 156 from their choice of friction coefficient  $< 0.1$ ; adjusting their results to a friction coef-  
 157 ficient of 0.6 raises their estimate of thermal anomaly to values consistent with most of  
 158 the other studies. Zhang & Sagiya (2017) include both frictional and viscous shear heat-  
 159 ing in their model, in which earthquakes are kinematically imposed and the depth of the  
 160 BDT is both gradual and determined self-consistently as part of the solution. They find  
 161 that for a continental strike-slip fault, the overall thermal anomaly peaks at roughly 200 °C  
 162 at about 12 km depth, which is sufficient to produce a shallower BDT than in an oth-  
 163 erwise equivalent model without shear heating. Lambert & Barbot (2016b) also account  
 164 for both frictional and viscous shear heating, modeling a fault with rate-and-state fric-  
 165 tion embedded in an elastic layer overlying a viscoelastic half-space. They find the mag-  
 166 nitude of the overall thermal anomaly to be on the order of 100-200 °C, centered in the  
 167 middle of the 15-km-deep velocity-weakening zone. Both Zhang & Sagiya (2017) and Lam-  
 168 bert & Barbot (2016b) find that frictional shear heating is larger than viscous shear heat-  
 169 ing, a result which might differ if dynamic weakening were included in the coseismic pe-  
 170 riod.

171 In this study, we develop and utilize a thermomechanical earthquake sequence model  
 172 which simulates earthquake cycles with a rate-and-state frictional fault in viscoelastic  
 173 half-space obeying a temperature-dependent power-law rheology. The mechanics prob-

174 lem is coupled to the heat equation with frictional and viscous shear heating source terms.  
 175 Our primary focus is on representing the BDT zone as a broad region whose depth is  
 176 not imposed a priori, but rather emerges from the solution of the governing equations  
 177 and changes in response to variable stresses and shear heating. In order to focus on temperature-  
 178 dependent effects, we consider a single frictional and compositional structure. We per-  
 179 form a parameter-space study exploring the influence of the ambient geotherm, param-  
 180 eterized by the lithosphere-asthenosphere boundary (LAB) depth; pore fluid pressure,  
 181 parameterized with the Hubbert-Rubey fluid pressure ratio; and the width of the fric-  
 182 tional shear zone. Shallower LAB depths correspond to warmer ambient geotherms, which  
 183 decrease the effective viscosity, producing a shallower BDT. Elevating pore fluid pres-  
 184 sure reduces the effective normal and shear stress on the fault, thereby decreasing fric-  
 185 tional shear heating. The lower shear strength of the fault also reduces deviatoric stresses  
 186 in the off-fault material, hence lowering viscous shear heating as well. Increasing the width  
 187 of the frictional shear zone decreases the local temperature rise (within a few meters of  
 188 the fault) produced by frictional shear heating, but otherwise results in minimal changes  
 189 in the model behavior.

## 190 2 Model

191 We model a vertical strike-slip fault in a viscoelastic half-space undergoing two-  
 192 dimensional antiplane shear deformation (Figure 1). The fault is located at  $y = 0$ , where  
 193  $y$  is horizontal and  $z$  is vertical and pointing down, with the origin located at the inter-  
 194 section of the fault with the Earth’s surface. To reduce computational cost, we use ma-  
 195 terial properties and tectonic loading that are symmetric about the fault, allowing us to  
 196 model only half of the domain ( $y \geq 0$ ). In this study, we use the quasi-dynamic approx-  
 197 imation to elastodynamics (i.e., quasi-static deformation with the radiation damping ap-  
 198 proximation, Rice, 1993), but future efforts can account for full elastodynamics as we  
 199 have demonstrated in another study that utilizes the same code (Duru et al., 2019). The  
 200 fault exists through the entire model domain so that the depth of the BDT, and the par-  
 201 titioning of tectonic loading into fault slip and bulk viscous flow, can be determined by  
 202 the depth-dependent relative strength of the fault and off-fault material, rather than be-  
 203 ing imposed a priori. Below we state the governing equations and boundary conditions.

204 The static equilibrium equation is

$$205 \quad \frac{\partial \sigma_{xy}}{\partial y} + \frac{\partial \sigma_{xz}}{\partial z} = 0, \quad (1)$$

206 where  $\sigma_{ij}$  are the quasi-static stress components, which are given by Hooke’s law,

$$207 \quad \sigma_{xy} = \mu \left( \frac{\partial u}{\partial y} - \gamma_{xy}^V \right), \quad \sigma_{xz} = \mu \left( \frac{\partial u}{\partial z} - \gamma_{xz}^V \right), \quad (2)$$

208 where  $u$  is the displacement in the  $x$  direction,  $\gamma_{ij}^V$  are the (engineering) viscous strains,  
 209 and  $\mu$  is the shear modulus. The viscous strains are determined by the power-law vis-  
 210 cous flow law

$$211 \quad \dot{\gamma}_{xy}^V = \eta_{\text{eff}}^{-1} \sigma_{xy}, \quad \dot{\gamma}_{xz}^V = \eta_{\text{eff}}^{-1} \sigma_{xz}, \quad (3)$$

$$212 \quad \eta_{\text{eff}}^{-1} = A e^{-Q/RT} \bar{\tau}^{n-1}, \quad \bar{\tau} = \sqrt{\sigma_{xy}^2 + \sigma_{xz}^2}, \quad (4)$$

214 where the overdot indicates a time derivative,  $\eta_{\text{eff}}$  is the effective viscosity,  $T$  is the tem-  
 215 perature, and  $R$  is the universal gas constant. The effective viscosity is a nonlinear func-  
 216 tion of the deviatoric stress invariant  $\bar{\tau}$ , and also depends upon several rheological pa-  
 217 rameters which vary with composition: the rate coefficient  $A$ , the activation energy  $Q$ ,  
 218 and the stress exponent  $n$ . Deviatoric stresses and in-plane viscous flow are neglected.

219 On the fault, frictional strength (i.e., the shear resistance to sliding),  $\tau$ , balances  
 220 the resolved shear traction on the fault, accounting for the radiation-damping response

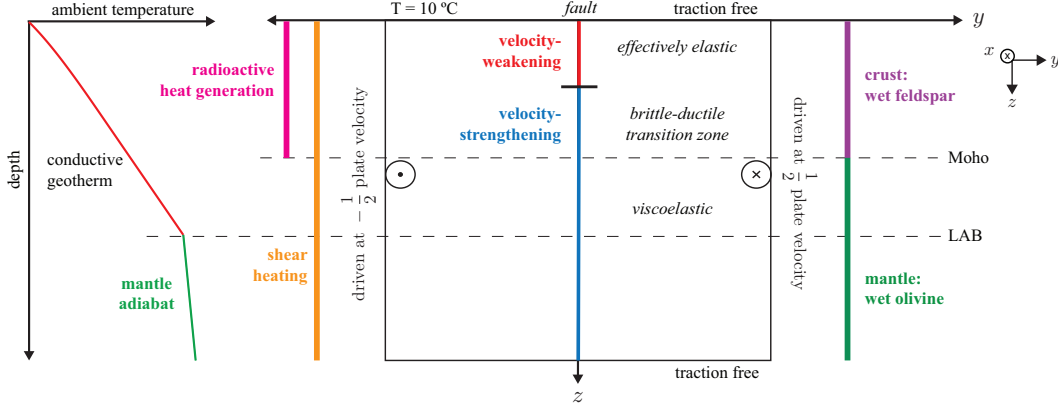


**Figure 1.** Our 2D strike-slip fault model simultaneously captures the transition from velocity-weakening (VW) to velocity-strengthening (VS) rate-and-state friction and the off-fault transition from effectively elastic to viscoelastic deformation. The depths of both transitions depend on temperature, so we consider a range of ambient geotherms, using a conductive geotherm in the crust and an adiabat below the lithosphere-asthenosphere boundary (LAB). We also account for thermal anomalies arising from frictional and viscous shear heating by simultaneously solving the heat equation.

221 (Rice, 1993):

$$222 \quad \tau(z, t) = \sigma_{xy}(0, z, t) - \eta_{rad}V = f(\psi, V)\bar{\sigma}_n, \quad (5)$$

$$223 \quad \dot{\psi} = G(\psi, V), \quad (6)$$

$$224 \quad \delta(z, t) \equiv 2u(0, z, t), \quad (7)$$

$$225 \quad V \equiv \frac{\partial \delta}{\partial t}. \quad (8)$$

226  
227 where  $\bar{\sigma}_n$  is effective normal stress,  $\psi$  is the state variable,  $V$  is slip velocity,  $\delta$  is slip, and  
228  $f$  is the friction coefficient. Equation (6) is the state evolution equation, e.g., either the  
229 slip law or the aging law (in this study we use the aging law).

230 Boundary conditions on the exterior sides of the domain are

$$231 \quad \sigma_{xz}(y, 0, t) = 0, \quad (9)$$

$$232 \quad \sigma_{xz}(y, L_z, t) = 0, \quad (10)$$

$$233 \quad u(L_y, z, t) = \frac{V_L t}{2} \quad (11)$$

234  
235 where  $L_y$  and  $L_z$  are the dimensions of the model domain in the  $y$ - and  $z$ -directions,  
236 respectively, and  $V_L$  is the tectonic plate (i.e., loading) velocity. At Earth's surface, we  
237 use a traction-free boundary condition (9). We also use this boundary condition at the  
238 bottom of the domain, because it permits an arbitrary amount of displacement to oc-  
239 cur. This is necessary for elastic models, but is irrelevant in viscoelastic models, as vis-  
240 cous flow permits arbitrary displacements at the bottom of the domain as well. Tectonic  
241 loading displacement is applied at a steady rate to the lateral boundary. It is important  
242 to use a sufficiently large domain such that the model behavior is independent of  $L_y$  or  
243  $L_z$  (Erickson et al., 2020), so we place both boundaries at 500 km, or about 50 times the  
244 seismogenic depth, using a coordinate transform (i.e., grid stretching) for computational  
245 efficiency (Allison & Dunham, 2018).

246 We additionally solve the energy balance or heat equation for the perturbation  $\Delta T$ ,  
247 or thermal anomaly, from the ambient one-dimensional geotherm  $T_{amb}$ . Above the LAB,

248  $T_{\text{amb}}$  corresponds to steady-state vertical conduction with radiogenic heat generation in  
 249 the crust, and below the LAB it follows the mantle adiabat (Turcotte & Schubert, 2002):

$$250 \quad \frac{d}{dz} \left( k \frac{dT_{\text{amb}}}{dz} \right) + Q_{\text{rad}} = 0, \quad 0 < z < z_{\text{LAB}}, \quad (12)$$

$$251 \quad Q_{\text{rad}} = A_0 e^{-z/d_r}, \quad (13)$$

$$252 \quad T_{\text{amb}}(y, 0, t) = T_0 \quad (14)$$

$$253 \quad T_{\text{amb}}(z_{\text{LAB}}) = T_p + gz_{\text{LAB}}, T_{\text{amb}}(z) = T_p + gz, \quad z \geq z_{\text{LAB}}, \quad (15)$$

255 where  $Q_{\text{rad}}$  is the source term for radiogenic heat generation in the crust,  $T_p$  is the man-  
 256 tle potential temperature, and  $g$  is the slope of the mantle adiabat. To solve for  $T_{\text{amb}}$   
 257 above the LAB, we hold the temperature at the Earth's surface fixed at  $T_0 = 10^\circ\text{C}$ ,  
 258 and at  $z_{\text{LAB}}$  the temperature is determined by the mantle adiabat.

259 The heat equation for the thermal anomaly  $\Delta T$ , which is solved over the entire do-  
 260 main (both above and below the LAB) is

$$261 \quad \rho c \frac{\partial \Delta T}{\partial t} = \frac{\partial}{\partial y} \left( k \frac{\partial \Delta T}{\partial y} \right) + \frac{\partial}{\partial z} \left( k \frac{\partial \Delta T}{\partial z} \right) + Q_{\text{visc}} + Q_{\text{fric}}, \quad (16)$$

$$262 \quad Q_{\text{visc}} = \bar{\tau} \dot{\gamma}^V, \quad Q_{\text{fric}} = \frac{\tau V}{\sqrt{2\pi w}} \exp\left(\frac{-y^2}{2w^2}\right), \quad (17)$$

264 where  $\rho$  is the density,  $c$  is the specific heat,  $\dot{\gamma}^V = \sqrt{(\dot{\gamma}_{xy}^V)^2 + (\dot{\gamma}_{xz}^V)^2}$  is the second in-  
 265 variant of the viscous strain rate, and  $Q_{\text{visc}}$  and  $Q_{\text{fric}}$  are the source terms for viscous  
 266 and frictional shear heating, respectively. We spread frictional shear heating over a Gaus-  
 267 sian shear zone of half width  $w$  (e.g., Andrews, 2002; Rice, 2006), which we vary from  
 268 0.1 to 10 m. Geologic observations indicate that, in the shallow crust and for an indi-  
 269 vidual earthquake, this frictional shear zone can be as narrow of tens of micrometers,  
 270 suggesting that frictional shear heating could instead be included as a heat flux radiat-  
 271 ing from a planar fault (Rice, 2006). However, without the inclusion of a dynamic weak-  
 272 ening mechanism such as thermal pressurization or flash heating, this would result in an  
 273 unrealistically large coseismic temperature rise and the onset of melting (Rempel & Rice,  
 274 2006), which is neglected in our model. Our model can easily be extended to include dy-  
 275 namic weakening, but this would introduce additional free parameters and complexity,  
 276 so we defer this important extension to future studies.

277 With regard to boundary conditions for  $\Delta T$ , we hold the exterior boundaries fixed  
 278 at the temperature of the ambient geotherm, and account for frictional heating only through  
 279 a source term as described above:

$$280 \quad \frac{\partial \Delta T}{\partial y} \Big|_{y=0} = 0, \quad \Delta T(L_y, z, t) = 0, \quad \Delta T(y, 0, t) = 0, \quad \Delta T(y, L_z, t) = 0. \quad (18)$$

281 As in the mechanical problem, it is important that the domain is large enough that the  
 282 thermal anomaly is not impacted by the remote boundary conditions. We use the same  
 283 domain for both the heat equation and the mechanical problem, so this condition is eas-  
 284 ily satisfied.

285 The discretization of the governing equations is described in the Supporting Infor-  
 286 mation. The grid spacing in the  $z$ -direction is chosen to resolve frictional dynamics. We  
 287 also use a grid spacing of  $w/5$  (0.02 m) in the  $y$ -direction near the fault to resolve ther-  
 288 mal boundary layers that arise during the coseismic phase. Grid stretching is used away  
 289 from the fault and seismogenic zone.

## 290 **2.1 Ambient Geotherms**

291 The power-law rheology is strongly temperature-dependent, and therefore the choice  
 292 of ambient geotherm makes a significant difference in the behavior of the system. We

parameter	symbol	value
<i>Frictional parameters</i>		
direct effect parameter	$a$	depth variable, see Figure 3a
state evolution effect parameter	$b$	depth variable, see Figure 3a
state evolution distance	$d_c$	3.2, 6.3, 10 mm
reference friction coefficient for steady sliding	$f_0$	0.6
reference velocity	$V_0$	$10^{-6}$ m/s
radiation damping coefficient	$\eta_{rad}$	4.68 MPa s/m
Hubbert-Rubey pore pressure ratio	$\lambda$	0.8, 0.6, 0.37
effective normal stress	$\bar{\sigma}_n$	depth variable, see Figure 3c
nucleation zone size	$h^*$	5 km at 12 km
<i>Viscoelastic parameters</i>		
shear modulus	$\mu$	30 GPa
density	$\rho$	2700 kg/m <sup>3</sup>
loading velocity	$V_L$	$10^{-9}$ m/s
Moho depth	$z_{\text{Moho}}$	30 km
<i>Thermal parameters</i>		
surface radiogenic heat production rate per unit mass	$A_0$	$2 \mu\text{W}/\text{m}^2$
length scale for radiogenic heat generation	$d_r$	10 km
mantle adiabat	$g$	$0.3^\circ\text{C}/\text{km}$
thermal conductivity	$k$	$2.5 \text{ W}/\text{m}/\text{K}$
Earth's surface temperature	$T_0$	$10^\circ\text{C}$
mantle potential temperature	$T_p$	$1200^\circ\text{C}$
frictional shear zone width	$w$	0.1 - 10 m
LAB depth	$z_{\text{LAB}}$	40 - 70 km
thermal diffusivity	$\alpha_{th}$	$1 \text{ mm}^2/\text{s}$
heat capacity	$\rho c$	$2.5 \text{ MJ}/^\circ\text{C m}^3$

**Table 1.** Model parameters. Note that state evolution distance  $d_c$  is varied with pore pressure ratio  $\lambda$  in order to keep nucleation length unchanged.

293 consider four candidate geotherms (Figure 2), selected to be representative of southern  
 294 California. The geotherms are consistent with observations of surface heat flow of 60-  
 295 120 mW/m<sup>2</sup> (Lachenbruch et al., 1985; Williams & DeAngelo, 2011) and estimates of  
 296 the Moho temperature of 650-850 °C (Humphreys & Hager, 1990; Yang & Forsyth, 2008).  
 297 Exhumed xenoliths originating from a few kilometers below the Moho in the Mojave re-  
 298 gion are consistent with the upper end of this Moho temperature range (Behr & Hirth,  
 299 2014). The geotherms are constructed assuming a surface temperature of 10°C, a man-  
 300 tle adiabat of 0.3°C/km, and mantle potential temperature of 1200°C (Lachenbruch &  
 301 Sass, 1977). Radiogenic heat generation is included only in the crust above the LAB, with  
 302 the heat production decaying exponentially with depth, as defined in Equation (13) (Lachen-  
 303 bruch & Sass, 1977). Based on Lekic et al. (2011), we consider four LAB depths: 40, 50,  
 304 60, and 70 km. For simplicity, we assume constant thermal parameters throughout the  
 305 domain, given in Table 1 (Turcotte & Schubert, 2002).

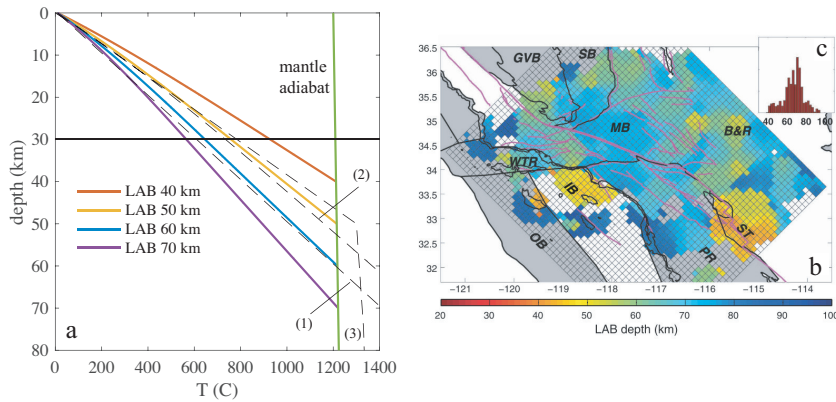


**Figure 2.** (a) Ambient geotherms constructed using a conductive geotherm in the lithosphere, including radiogenic heat generation in the crust, and a mantle adiabat, representative of a convective regime. The LAB is the depth at which the conductive geotherm intersects the mantle adiabat. We consider four LAB depths: 40, 50, 60, and 70 km. The dashed black lines show geotherms used in other, similar studies: (1) Takeuchi & Fialko (2012), (2) Sass et al. (1997), and (3) Freed & Bürgmann (2004) and Takeuchi & Fialko (2013). (b) and (c) LAB depths in southern California, reproduced from Lekic et al. (2011).

## 306 2.2 Rheological Parameters

307 We consider a single, layered composition, representing the crust with wet feldspar  
 308 and the mantle with wet olivine. The transition in composition from the crust to the man-  
 309 tle occurs smoothly over 10 km, as shown in Figure 3b, using a mixing law representa-  
 310 tive of magmatic underplating, as in Allison & Dunham (2018). Also, we neglect spa-  
 311 tial variation in the shear modulus, instead using the constant value given in Table 1.  
 312 We assume the viscous deformation mechanisms to be dislocation creep in both the crust  
 313 and mantle, though there is evidence that feldspar in the lower crust deforms through  
 314 diffusion creep as well, particularly in shear zones where the grain size is reduced (Ry-  
 315 backi & Dresen, 2004). While our method can handle diffusion creep and different rheo-  
 316 logies in shear zones, we defer this to future work (Allison & Montesi, 2020).

## 317 2.3 Stress State

318 The frictional strength of the fault (5) is intimately related to the stress state of  
 319 the system, which is essential to specify given the nonlinearity of the viscous flow law

material	A (MPa <sup>-n</sup> s <sup>-1</sup> )	n	Q (kJ mol <sup>-1</sup> )	source
wet feldspar	$1.58 \times 10^3$	3	345	Rybacki et al. (2006)
wet olivine	$3.6 \times 10^5$	3.5	480	Hirth & Kohlstedt (2003)

**Table 2.** Values used for power-law flow parameters.

and rate-and-state friction law. We set the overall stress state, which enters our model solely through the effective normal stress on the fault in equation (5), by assuming an optimally oriented strike-slip fault having friction coefficient  $f_0 = 0.6$  (e.g., Sibson, 1974). We assume vertical total stress is equal to lithostatic pressure, and consider different conditions for pore pressure at depth, parameterized with the Hubbert-Rubey fluid pressure ratio  $\lambda$  (equal to pore pressure divided by lithostatic pressure) (Hubbert & Rubey, 1959).

We first consider the case of hydrostatic pore pressure,  $\lambda = 0.37$  for the rock density used in this study. We also consider two cases of elevated pore pressure:  $\lambda = 0.6$  and  $0.8$ . Note that this background stress state produces both antiplane and in-plane deviatoric stresses. As explained earlier, we neglect the contribution of in-plane deviatoric stresses in our application of the viscous flow law, such that the resulting deformation is exclusively 2D antiplane shear. This does limit the applicability of our results for certain applications, such as quantifying the orientation and relative magnitude of the principal stresses, which require fully 3D calculations.

#### 2.4 Frictional Parameters

The frictional strength of the fault is governed by rate-and-state friction. We use the regularized form (Rice et al., 2001),

$$f(\psi, V) = a \sinh^{-1} \left( \frac{V}{2V_0} e^{\psi/a} \right) \approx a \ln \left( \frac{V}{V_0} \right) + \Psi, \quad (19)$$

with the aging law for state evolution (Ruina, 1983; Marone, 1998),

$$G(\psi, V) = \frac{bV_0}{d_c} \left( e^{(f_0 - \psi)/b} - \frac{V}{V_0} \right). \quad (20)$$

This formulation can be brought into the more common form of rate-and-state friction by replacing our choice of (dimensionless) state variable,  $\Psi$ , with the usual state variable  $\theta$  (having units of time) via  $\Psi = f_0 + b \ln(V_0\theta/d_c)$ , such that  $f \approx f_0 + a \ln(V/V_0) + b \ln(V_0\theta/d_c)$  and  $G = 1 - V\theta/d_c$ . However,  $\Psi$ , as a nondimensional quantity of order unity, is better suited for numerical calculations. The primary parameters which determine the frictional behavior of the system are the direct effect parameter  $a$ , the state evolution parameter  $b$ , and the state evolution distance  $d_c$ . Velocity-weakening (VW) regions with  $a - b < 0$  have the potential for unstable sliding, where velocity-strengthening (VS) regions with  $a - b > 0$  generally slip aseismically unless forced by a dynamic rupture. Due to the increase in temperature with depth, friction transitions from VW to VS with increasing depth. This transition in frictional behavior may control the down-dip limit of ruptures; however, the experimental results of Mitchell et al. (2016), performed up to 600°C on granite, suggest that friction may remain VW to the depth of the BDT for most geotherms. In this case, the down-dip limit of ruptures would be determined by the BDT instead.

To set the depth dependence of  $a$  and  $b$ , we use laboratory data for wet granite gouge from Blanpied et al. (1991, 1995), reproduced in Figure 3a. The wet granite data have been used extensively in earthquake cycle simulations (e.g., Rice, 1993; Lapusta et al.,

2000; Lapusta & Rice, 2003b; Kato, 2002; Lindsey & Fialko, 2016; Allison & Dunham, 2018). The data predict a shallow transition from VS to VW at about 100°C and a deeper transition back to VS at around 350°C; however, as our focus is on the behavior of the system at depth, we neglect the shallow transition. To assign depth dependence of frictional properties from temperature-dependent data, we use the ambient geotherm for a 60 km deep LAB. For simplicity, we use the same depth distribution of frictional properties for all simulations. We also neglect changes in frictional parameters as a result of the changes in temperature produced by shear heating. Since the fault exists through the entire depth of the model, we use linear extrapolation to assign values below the last data point, based on the theoretically expected linear dependence of  $a$  on temperature (Rice et al., 2001). For  $d_c$ , laboratory data indicates that it is on the order of a few to tens of microns (e.g., Dieterich, 1979; Marone & Kilgore, 1993); however, to reduce the computational expense, we use  $d_c = 10$  mm in the model with hydrostatic pore pressure. This corresponds to a 5 km nucleation zone, estimated as  $h^* = \mu d_c / (\bar{\sigma}_n (b - a))$ , at 12 km depth (the approximate depth of nucleation in elastic models with these parameters). We change  $d_c$  to keep  $h^*$  constant at this depth in models with elevated pore pressure. More details are provided in Supporting Information.

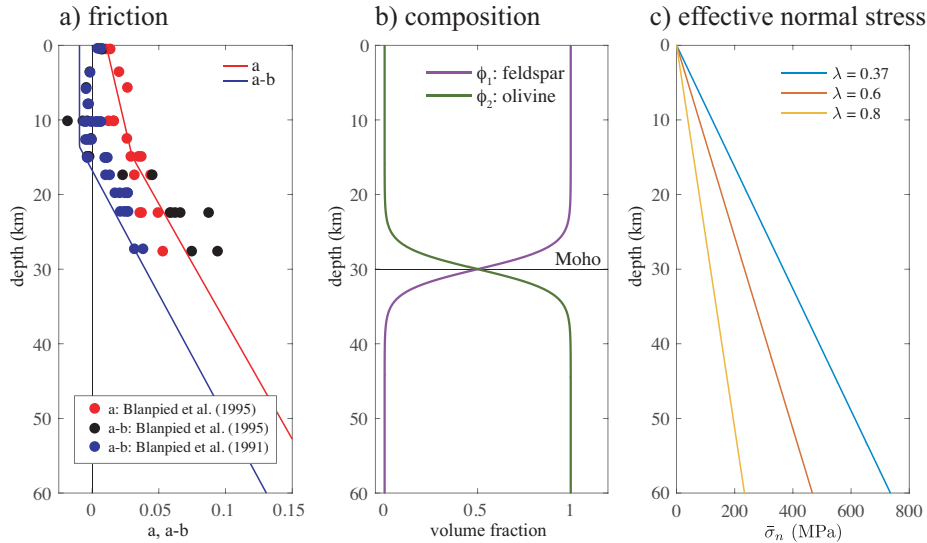


**Figure 3.** (a) Rate-and-state laboratory data for  $a$  and  $a-b$  for wet granite from Blanpied et al. (1991, 1995) shown as dots, and model parameters shown as solid lines. The data have been converted from temperature to depth using a the geotherm for a 60 km deep LAB. (b) Volume fractions for feldspar and olivine, smoothly transitioning across the Moho depth of 30 km. (c) Effective normal stress for varying pore pressure:  $\lambda = 0.37$  (hydrostatic pore pressure), 0.6, and 0.8.

### 3 Results

We first illustrate the effects of shear heating and viscous flow on the earthquake cycle by presenting results from a representative viscoelastic earthquake cycle simulation with shear heating. Results from this simulation are compared with those from an otherwise identical viscoelastic simulation with no shear heating, in which temperature is fixed to the ambient geotherm, and an elastic simulation. Then, we present results from our steady-state simulations, which characterize many features of the system, such as

383 the depth of the BDT and the stress distribution through the lithosphere. We also dis-  
 384 cuss the relative contributions of frictional and viscous shear heating, showing that both  
 385 are of roughly equal magnitude. Finally, we summarize results of a parameter-space study  
 386 varying the ambient geotherm (i.e., LAB depth), pore fluid pressure ratio  $\lambda$ , and fric-  
 387 tional shear zone width, exploring how these parameters control characteristics of the  
 388 earthquake cycle and the BDT depth.

### 389 3.1 Representative Viscoelastic Cycle Simulation with Shear Heating

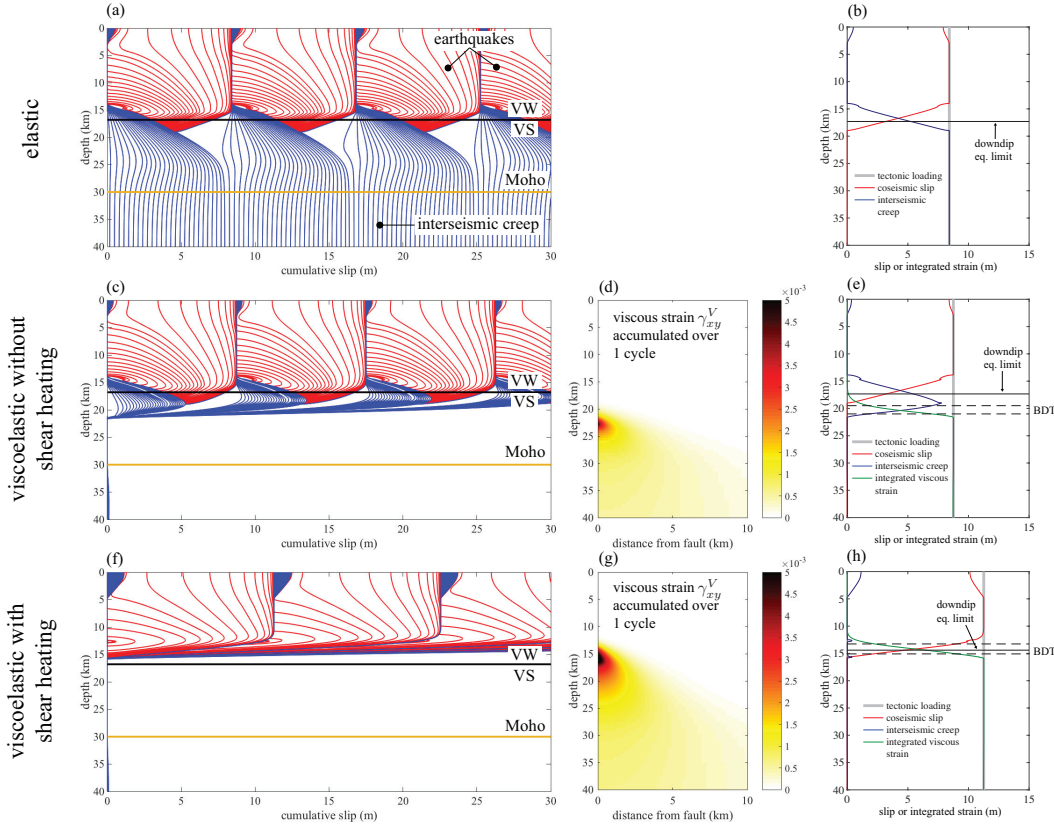


**Figure 4.** Comparison between elastic (top row), viscoelastic without shear heating (middle row), and viscoelastic with shear heating (bottom row) cycle simulations for a 50 km deep LAB, hydrostatic pore pressure, and  $w = 1$  m. (a), (c), and (f) Cumulative slip, plotted in red every 1 s for coseismic slip and in blue every 10 years during the interseismic period. Shear heating shallows the earthquake cycle and the BDT. (d) and (g) Viscous strain  $\gamma_{xy}^V$  accumulated over one earthquake cycle. (b), (e), and (h) Partitioning of tectonic loading (grey) into coseismic slip (red), interseismic slip (blue), and bulk viscous flow (green, obtained by integrating  $\gamma_{xy}^V$  over horizontal lines at fixed depth). Also shown are the down-dip limit of the earthquake (black, solid) and depth of the BDT (black, dashed).

390 In this section, we summarize the results from a representative viscoelastic cycle  
 391 simulation with shear heating with a 50 km deep LAB, hydrostatic pore pressure ( $\lambda =$   
 392 0.37), and a  $w = 1$  m wide frictional shear zone. Figure 4 compares the viscoelastic cy-  
 393 cle simulation with shear heating with equivalent viscoelastic without shear heating and  
 394 elastic simulations; additional details are given in Supporting Information (specifically,  
 395 Figure S1). In the elastic simulation (Figures 4a and b) the depths of earthquake nu-

396 cleation and down-dip propagation are determined by the VW-VS transition. Deeper  
 397 in the crust, tectonic loading is accommodated by frictional afterslip and interseismic  
 398 fault creep. The depths of earthquake nucleation and down-dip propagation are the same  
 399 in the viscoelastic simulation without shear heating (Figures 4c-e), and in fact the tran-  
 400 sition between coseismic and interseismic slip in the mid-crust is also very similar to that  
 401 of the elastic simulation. This echoes results of our previous study (Allison & Dunham,  
 402 2018). In contrast, in the viscoelastic cycle simulation with shear heating (Figures 4f-  
 403 h), coseismic slip is confined to shallower depths, because it is limited not by the tran-  
 404 sition in frictional properties but by the BDT.

405 In both viscoelastic simulations, tectonic loading in the lower crust is accommo-  
 406 dated by off-fault viscous flow (Figures 4d and g). Viscous flow is concentrated near the  
 407 fault at the depth at which fault slip ceases, and becomes more broadly distributed with  
 408 depth. Shear heating produces only a slightly more localized shear zone, at least for the  
 409 chosen parameters and rheology.

410 Comparing the cumulative slip plot for the viscoelastic cycle simulation with shear  
 411 heating (Figure 4f), with that for the viscoelastic cycle simulation without shear heat-  
 412 ing (Figure 4c), it is evident that shear heating shallows the depth of earthquake nucle-  
 413 ation and the down-dip limit of coseismic slip. However, the total coseismic slip per event  
 414 is larger because the recurrence interval is larger.

415 Since these simulations are in a limit cycle, producing the same earthquake cycle  
 416 periodically, the elastic strain in the system returns to the same level after each cycle  
 417 (Savage & Prescott, 1978). Therefore, the tectonic loading displacement over one cycle  
 418 is partitioned into coseismic and interseismic fault slip, and viscous flow:

$$419 \quad \delta_{\text{co}} + \delta_{\text{int}} + \int_{-L_y}^{L_y} \gamma_{xy}^V dy = V_L T_{\text{rec}} \quad (21)$$

420 where  $\delta_{\text{co}}$  is the coseismic slip,  $\delta_{\text{int}}$  is the interseismic slip, and  $T_{\text{rec}}$  is the recurrence in-  
 421 terval. Figures 4b, e, and h show the depth dependence of this partitioning. The solid  
 422 black line shows a measure of the down-dip limit of coseismic slip, defined as the depth  
 423 above which 98% of the total potency of the earthquake occurs. The dashed black lines  
 424 show a measure of the depth of the BDT zone, defined as the depths between which 20%  
 425 and 80% of the tectonic loading is accommodated by bulk viscous flow. In this case, the  
 426 inclusion of shear heating shallows the BDT by about 5 km, causing it to overlap with  
 427 the down-dip limit of coseismic slip, producing a 1.2-km-wide region in which one might  
 428 find geologic evidence of both brittle and ductile deformation. This is discussed in greater  
 429 detail in Section 3.3.

430 Figure 5 shows the thermal anomaly from shear heating,  $\Delta T$ . The thermal anomaly  
 431 from frictional shear heating during the coseismic phase persists into the early postseis-  
 432 mic period, lasting for about 1 month (Figure 5a-d). It is initially concentrated over dis-  
 433 tance  $w$  from the center of the fault zone, then diffuses outward. Though the thermal  
 434 anomaly produced by each earthquake is short-lived, a nonzero thermal anomaly per-  
 435 sists through the interseismic period (Figure 5e); this is the cumulative effect of a long  
 436 sequence of past earthquakes. Decreasing  $w$  causes the maximum transient thermal anomaly  
 437 to increase (Figure 5f), but we find that it is so short-lived and localized that  $w$  has neg-  
 438 ligible impact on characteristics of the earthquake cycle, such as the recurrence inter-  
 439 val, earthquake nucleation depth and down-dip limit, and BDT depth. For example, for  
 440 the simulation with a 50 km LAB,  $\lambda = 0.37$ , and  $w = 0.3$  m, the transient effect of  
 441 shear heating is to drop the effective viscosity in the mid-crust (10-15 km depth) within  
 442 0.5 m of the fault to about  $3 \times 10^{13}$  Pa s, which corresponds to a Maxwell time of 1000 s.  
 443 This causes viscous strain to accumulate in this region over the period of 1 day, corre-  
 444 sponding to an additional offset across the fault of 1.3 mm (only 0.025% of the total tec-  
 445 tonic offset over the cycle). Simulations with larger  $w$  produce smaller transient temper-  
 446 ature rises.

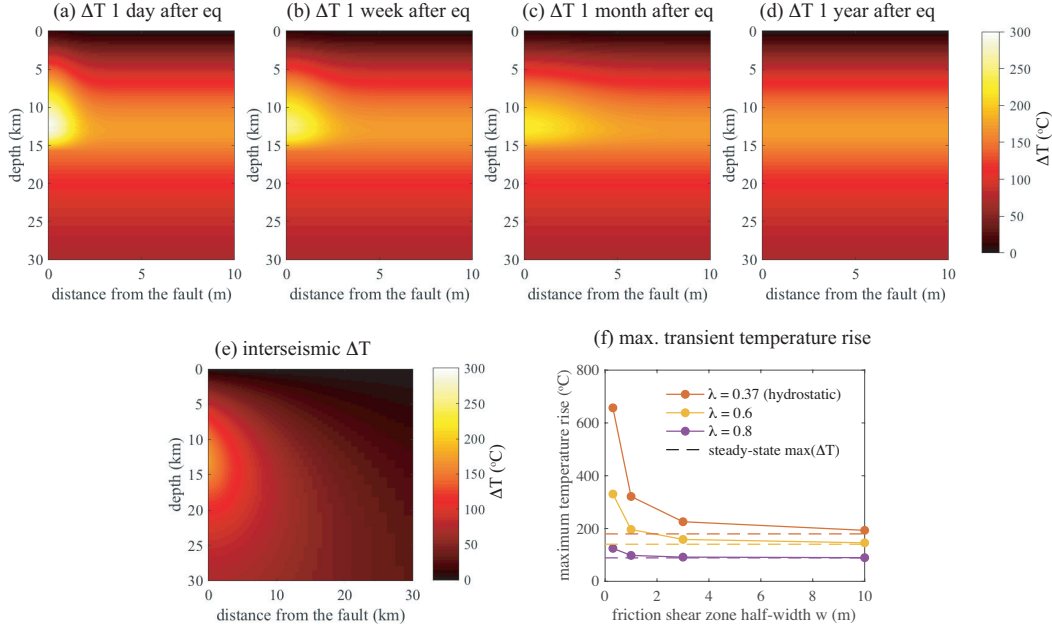


**Figure 5.** Evolution of thermal anomaly for the viscoelastic cycle simulation with shear heating with a 50 km deep LAB, hydrostatic pore pressure, and  $w = 1$  m. (a)-(d) Snapshots of the thermal anomaly within one year after the earthquake, showing that the thermal anomaly from frictional heat generation lasts for a very short period of time, relative to the recurrence interval, and is restricted to the middle crust between 10 and 15 km depth. (e) Corresponding average interseismic thermal anomaly. Note the change in  $x$ -axis from (a)-(d) to (e). (f) Maximum transient thermal anomaly increases as the frictional shear zone half-width  $w$  shrinks, with the maximum of the thermal anomaly from the steady-state model plotted (dashed) for reference.

447

### 3.2 Insight from Steady-State Results

448

449

450

451

452

453

454

455

456

457

458

459

In addition to viscoelastic cycle simulations with shear heating that resolve the transient slip dynamics (i.e., coseismic, postseismic, and interseismic phases), we also performed steady-state simulations in which fault slip velocity and off-fault viscous strain rates are constant in time (see Appendix A for details on the solution method). While this steady-state model is an approximation that neglects transient slip behavior like earthquakes, we find that it provides remarkably accurate predictions of the general lithospheric stress distribution, thermal anomaly, and heat flux. Therefore, in this section we use the steady-state model to explore the relative contributions of frictional and viscous shear heating to the thermal anomaly, and the effect of shear heating on the depth of the BDT. The frictional shear zone half-width  $w$  has no impact on these results within the range of  $w$  considered, because  $w$  is much smaller than the characteristic length scales of the heat generation region.

460

461

462

463

464

465

466

467

Shear heating significantly weakens the root of the fault and shallows the BDT, as illustrated in Figure 6. Weakening in the lower crust is greatest for simulations with low pore pressure and the coolest background geotherm. The case with an LAB depth of 50 km and hydrostatic pore pressure is explored in more detail in Figure 7a. The total thermal anomaly  $\Delta T$  is shown in Figure 7d, and the portions of that anomaly produced by frictional and viscous shear heating ( $\Delta T_{\text{fric}}$  and  $\Delta T_{\text{visc}}$ , respectively) are plotted in Figure 7e and f. This division is obtained by linearity of the heat equation, with  $\Delta T_{\text{fric}}$  and  $\Delta T_{\text{visc}}$  computed a posteriori from a simulation that includes both contributions. Both

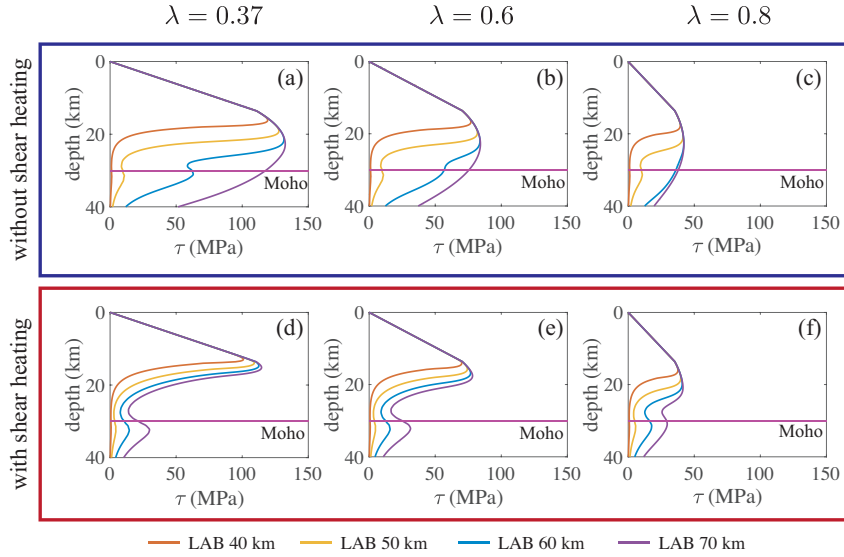


**Figure 6.** Shear stress on the fault and its deep extension for viscoelastic simulations with (right) and without (left) shear heating, with pore pressure increasing down the rows.

468 contributions to the total thermal anomaly are of roughly similar magnitude, though they  
 469 differ in spatial distribution. Frictional shear heating is most significant in the middle  
 470 of the crust where the shear stress and slip velocity are both high. In contrast,  $\Delta T_{\text{visc}}$   
 471 is concentrated at significantly greater depths because it is generated primarily at the  
 472 depth of the BDT, where the viscous strain rate is highest. It also occurs over a broader  
 473 spatial scale than frictional shear heating. Neglecting either frictional or viscous shear  
 474 heating, resulting in the red and yellow curves in Figure 7a and the thermal anomaly plot-  
 475 ted in Figure 7b and c, produces a smaller total thermal anomaly and therefore a deeper  
 476 BDT. While the spatial distribution of the thermal anomalies produced by each source  
 477 of shear heating are quite different, the shear stress profiles are relatively similar to each  
 478 other, and quite different from the model which accounts for both sources. The effect  
 479 of varying pore pressure on  $\Delta T_{\text{fric}}$  and  $\Delta T_{\text{visc}}$  is illustrated in the Supporting Informa-  
 480 tion (Figure S2). Increasing pore pressure decreases  $\Delta T$ ,  $\Delta T_{\text{fric}}$ , and  $\Delta T_{\text{visc}}$ ; however,  
 481  $\Delta T_{\text{fric}}$  decreases less rapidly than  $\Delta T_{\text{visc}}$ , and therefore constitutes a larger fraction of  
 482 the total thermal anomaly for high pore pressures.

### 483 3.3 Parameter Space Study

484 In this section, we return to the results of our cycle simulations, summarizing the  
 485 effects of shear heating on the depth of earthquake nucleation, the down-dip limit of co-  
 486 seismic slip, and the BDT. Additional results concerning thermal energy are shown in  
 487 the Supporting Information (Figure S3). We also include steady-state results for compar-  
 488 ison when appropriate. Figure 8 compares results for viscoelastic simulations with  
 489 and without shear heating, as a function of LAB depth and  $\lambda$ . Frictional shear zone width  
 490  $w$  does not change any of these characteristics, and is held fixed at  $w = 1$  m in the re-  
 491 sults to follow. The nucleation depth is the depth at which the slip velocity first reaches  
 492 coseismic levels, defined as 1 mm/s, consistent with the cumulative slip plots. We cal-  
 493 culate the BDT from the cycle simulation results as described in Section 3.1, and also  
 494 calculate the BDT depth range from the steady-state results, using the same definition.

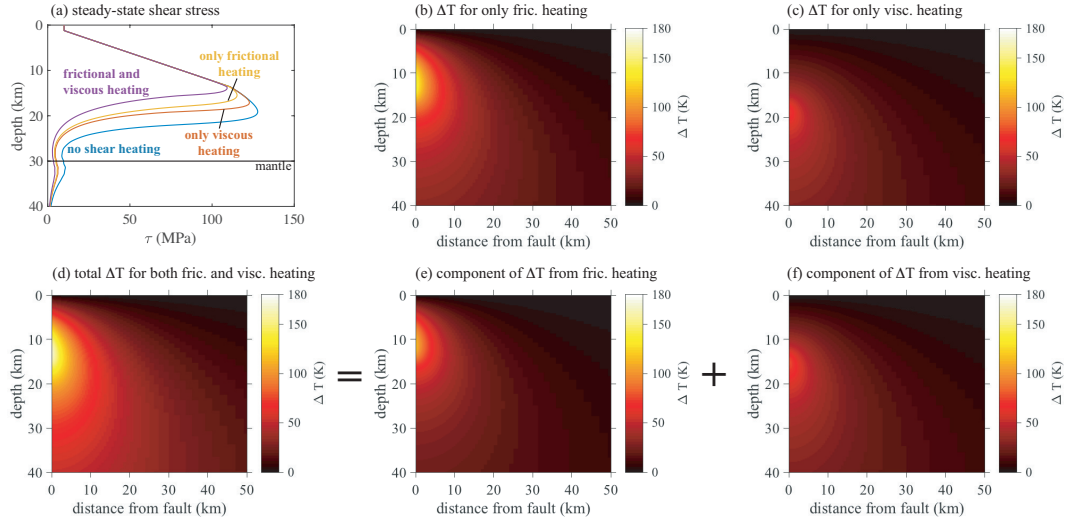


**Figure 7.** Results from steady-state model with an LAB at 50 km and hydrostatic pore pressure (all considered values of  $w$  produce these same results): (a) Shear stress on fault and its deep extension. (b)-(f) Thermal anomaly. (b) and (c) Thermal anomaly for simulations which include only frictional or viscous shear heating, respectively. (d) Total thermal anomaly for a simulation with both contributions to shear heating, and the portions of that anomaly which result from frictional and viscous shear heating are shown separately in (e) and (f). Frictional and viscous shear heating contribute relatively equally to the total thermal anomaly, and neglecting either one produces a much deeper BDT.

495 We also ran cycle simulations in which the transient effects of the cycles on the thermal  
 496 anomaly were neglected, in which we used a time-independent temperature distribution  
 497 taken from a corresponding steady-state simulation (thus accounting for the thermal anomaly  
 498 but not its time evolution over the cycle). These simulations produced such similar re-  
 499 sults to the results with transient shear heating that they are not plotted here.

500 Turning now to our results, the BDT is much shallower for all viscoelastic simu-  
 501 lations with shear heating than for corresponding simulations without shear heating. The  
 502 viscoelastic simulations with shear heating all predict a BDT in the middle to lower crust,  
 503 while many of the viscoelastic simulations without shear heating predict a BDT near or  
 504 below the Moho. Additionally, for simulations with and without shear heating, the BDT  
 505 becomes shallower for warmer geotherms (shallower LAB depths) and for decreasing pore  
 506 pressure. Warmer geotherms lead to lower effective viscosity, and therefore a shallower  
 507 BDT. Decreasing pore pressure leads to higher effective normal and shear stress on the  
 508 fault, more heat generated by frictional shear heating, and thus a shallower BDT. The  
 509 steady-state approximation for the BDT is quite accurate for most models, though it does  
 510 predict a slightly deeper BDT for some of the viscoelastic simulations without shear heat-  
 511 ing with elevated pore pressure.

512 The depths of earthquake nucleation and down-dip propagation can be controlled  
 513 by either the VW-VS transition on the fault, or the BDT. In the elastic simulations, there  
 514 is no BDT, and therefore the VW-VS transition determines both depths. The viscoelas-  
 515 tic simulations without shear heating produce very similar earthquake nucleation and  
 516 down-dip propagation depths to the elastic simulations, indicating that these depths are  
 517 also controlled by the VW-VS transition. In contrast, in the viscoelastic simulations with  
 518 shear heating the down-dip coseismic slip limit is sometimes determined by the BDT rather  
 519 than the VW-VS transition. For the parameters we consider, earthquakes never prop-

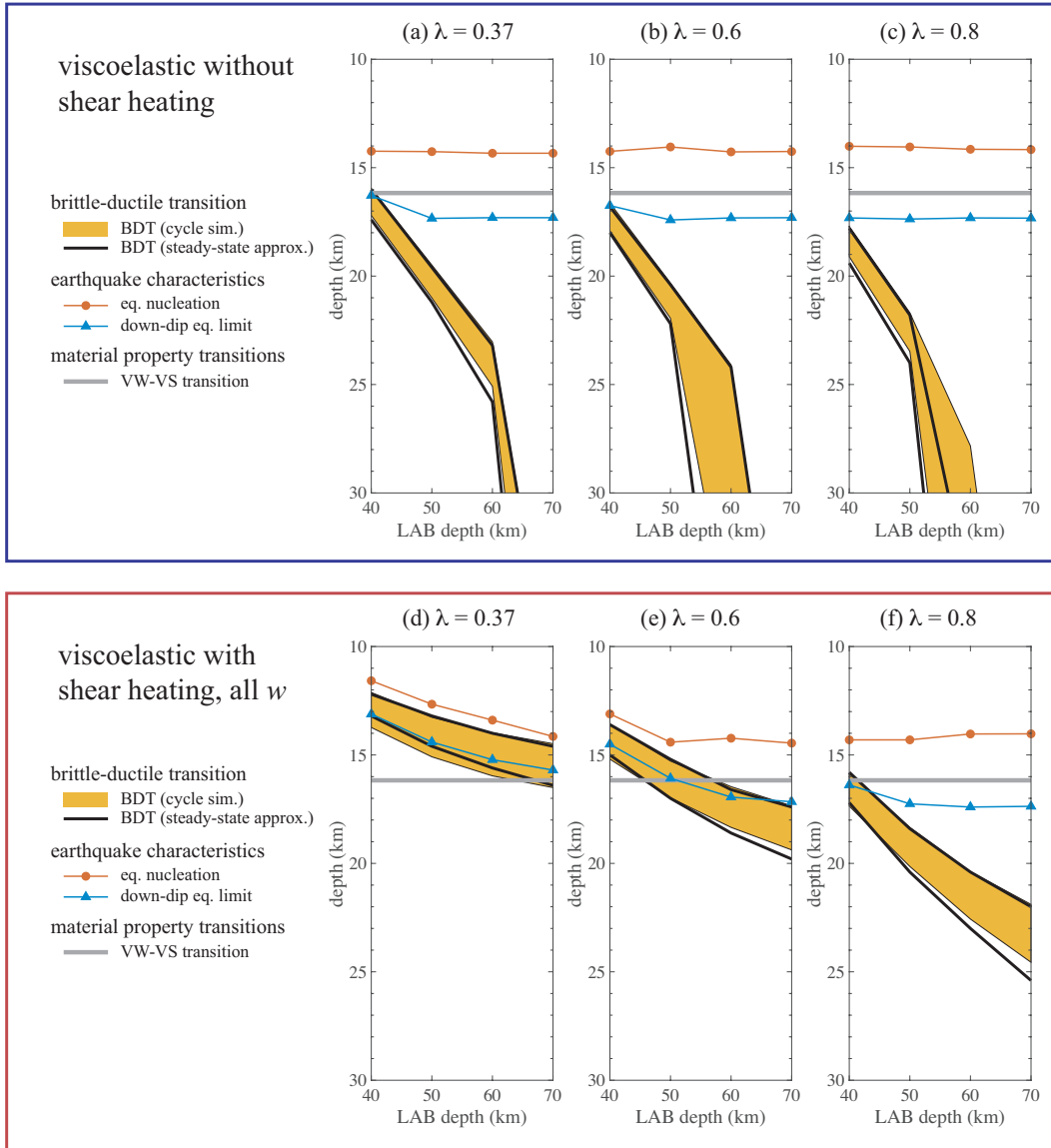


**Figure 8.** Comparison between earthquake nucleation depth (red circles), down-dip slip limit (blue triangles), and BDT depth range (yellow filled regions) for viscoelastic cycle simulations without (top row) and with (bottom row) shear heating. Also shown are estimates of the BDT from steady-state results (black lines).

520 agate all the way through the BDT. Therefore, when the BDT in the viscoelastic sim-  
 521 ulations with shear heating occurs above the down-dip coseismic slip limit in the elas-  
 522 tic simulations, coseismic slip is limited to shallower depths. The same applies to earth-  
 523 quake nucleation, which always occurs above the BDT. Thus, viscoelastic simulations  
 524 with shear heating with higher  $\lambda$  and shallower LAB depths have shallower BDTs, and  
 525 as a consequence shallower earthquakes.

526 We also find that the recurrence interval of the viscoelastic simulations with and  
 527 without shear heating sometimes differs from that of the equivalent elastic simulations.  
 528 For the viscoelastic simulations without shear heating, slow slip events occur between  
 529 the large earthquakes in some parts of parameter space (slow slip events do not occur

530 in the elastic simulations), and in these cases the recurrence interval is increased by as  
 531 much as 20 years. For viscoelastic simulations with shear heating, the recurrence inter-  
 532 val changes by tens to hundreds of years, with the largest changes occurring for low  $\lambda$   
 533 where  $\Delta T$  is largest; however, for some parameter choices, the recurrence interval is de-  
 534 creased while for others it is increased. For example, in Figure 4c, the recurrence inter-  
 535 val is about 100 years longer. We speculate that this effect is caused by a change in the  
 536 way remote loading is translated into loading of the seismogenic zone by deep viscous  
 537 flow and/or aseismic slip. Alternatively, changes in the effective seismogenic zone extent,  
 538 relative to the earthquake nucleation length, can influence recurrence interval dynam-  
 539 ics by the introduction or suppression of smaller ruptures (Cattania, 2019).

540 These results show that the inclusion of viscoelastic deformation can impact the  
 541 behavior of the seismogenic zone, such as nucleation depth and down-dip slip limit of  
 542 coseismic slip, but only when the BDT is shallow enough that appreciable viscous flow  
 543 occurs above the VW-VS transition. This explains why previous work on rate-and-state  
 544 cycle simulations in viscoelastic solids by Kato (2002) and Allison & Dunham (2018) found  
 545 that characteristics of the behavior of the seismogenic zone were not impacted by the  
 546 inclusion of viscoelastic deformation at depth. The geometry of an elastic layer over a  
 547 viscoelastic half-space used in Kato (2002) did not allow any overlap between the seis-  
 548 mogenic zone, which was confined within the elastic layer, and the deeper viscoelastic  
 549 half-space. And the simulations in Allison & Dunham (2018) were in a part of param-  
 550 eter space in which the BDT was much deeper than the seismogenic zone because shear  
 551 heating was not included, as in the viscoelastic simulations without shear heating shown  
 552 in this study.

553 The temperatures which correspond with the depths plotted in Figure 8 are shown  
 554 in Supporting Information (Figure S4). The steady-state approximation for the BDT is  
 555 again quite accurate. Additionally, the viscoelastic simulations with shear heating con-  
 556 sistent place the BDT at about 550–600°C. This is the temperature range in which,  
 557 for strain rates between  $10^{-14}$ – $10^{-12}$  s<sup>-1</sup>, the viscous strength of feldspar becomes weaker  
 558 than the frictional strength of the fault, shown in Figure 9. The viscoelastic simulations  
 559 without shear heating place in the BDT in the same 550–600°C range when it occurs  
 560 within the crust. These simulations place the BDT at a much higher temperature when  
 561 it occurs in the mantle because olvine has a larger dislocation creep activation energy  
 562 than feldspar, and a correspondingly higher BDT temperature.

### 563 3.4 Surface Heat Flux

564 Our model makes predictions of surface heat flux  $q$ , permitting comparison to mea-  
 565 surements. In Figure 10, we compare our steady-state surface heat flux predictions with  
 566 measurements for the creeping section of the San Andreas, near Parkfield (Fulton et al.,  
 567 2004). As expected, the magnitude of the predicted anomaly in  $q$  near the fault is smaller  
 568 for cooler ambient geotherms and elevated pore pressures. The ambient geotherm in this  
 569 region is best represented by our geotherms for LAB depths of 50 and 60 km (Sass et  
 570 al., 1997). There is a large amount of scatter in the data; however, it is clear that of the  
 571 simulations with both frictional and viscous shear heating considered here, only those  
 572 with substantially elevated fluid pressure ( $\lambda = 0.8$ ) can be considered consistent with  
 573 the data.

574 Elevated pore pressure has been suggested as a solution to the stress-heat flow para-  
 575 dox before (e.g., Byerlee, 1990; Rice, 1992; Tembe et al., 2009; Fulton & Saffer, 2009).  
 576 A number of alternative solutions for the paradox have also been proposed, however. In  
 577 particular, dynamic weakening reduces coseismic frictional heat generation, and can re-  
 578 duce the cycle-averaged thermal anomaly from frictional shear heating by allowing faults  
 579 to operate at lower background stress levels (Lapusta & Rice, 2003a). Our simulations  
 580 suggest that a weaker fault will also lead to smaller stresses in the off-fault material, and

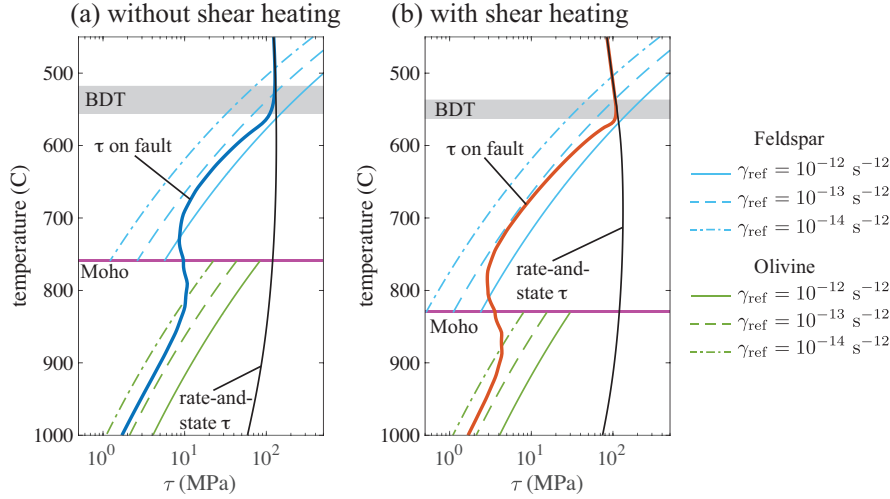


**Figure 9.** Comparison between shear stress on fault and predicted shear stress assuming a constant reference strain rate, for simulations with a 50 km deep LAB and hydrostatic pore pressure.

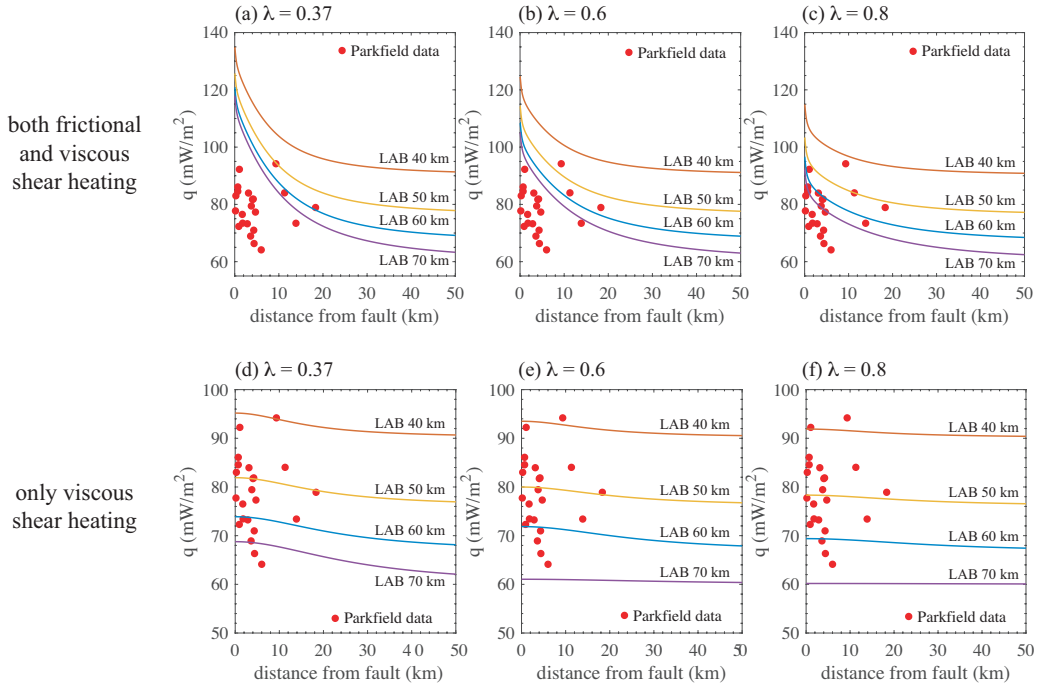


**Figure 10.** Comparison between surface heat flux simulation results (lines) and data (red points). (a) - (c) show results from simulations with both frictional and viscous shear heating. (d) - (f) show results from simulations with only viscous shear heating. Red points are measurements of heat flux as a function of distance from the San Andreas Fault, from Fulton et al. (2004). For the simulation results, the ambient geotherm determines the background heat flux far from the fault. Elevated pore pressure significantly reduces the magnitude of the anomaly near the fault.

581 to a smaller thermal anomaly from viscous shear heating as well. As a rough proxy for  
 582 the effect of dynamic weakening on frictional shear heating, neglecting its effects on the  
 583 long-term strength of the fault, we also consider simulations in which only viscous shear  
 584 heating is included, and frictional shear heating is neglected, in the bottom row of Fig-  
 585 ure 10. Because the thermal anomaly from viscous shear heating is relatively deep, the  
 586 magnitude of the peak in surface heat flux near the fault is smaller than the scatter in  
 587 the data. This suggests that, for simulations which do not produce clearly excessive heat  
 588 flux near the fault, whether through the inclusion of elevated pore pressure, dynamic weak-  
 589 ening, or another mechanism, it would be quite difficult to differentiate between mod-  
 590 els with surface heat flux data alone.

## 591 4 Discussion

### 592 4.1 Magnitude and Significance of Shear Heating

593 In this study, we quantified the effects of both frictional and viscous shear heat-  
 594 ing. Frictional shear heating produces transient changes in temperature in the mid-crust  
 595 in the coseismic and postseismic period, which for small shear zone widths  $w$  can reach  
 596 hundreds of degrees Celsius. But most results are insensitive to these temperature changes,  
 597 as a result of the short lifespan and limited spatial extent of the transient temperature  
 598 rise. Additionally, features like the interseismic thermal anomaly and the depth of the  
 599 BDT are well-characterized by a steady-state approximation, in which the effects of earth-  
 600 quake cycles are approximated with time-independent slip velocity and viscous strain  
 601 rates. Furthermore, cycle simulations which use the steady-state thermal anomaly and  
 602 neglect transient shear heating effects all together produce very similar system behav-  
 603 ior to those which include the transient effects, at a significant reduction in computa-  
 604 tional cost. These results demonstrate that viscous flow of the transiently thermally weak-  
 605 ened region immediately around the fault is unlikely to contribute to early postseismic  
 606 deformation, or be misinterpreted as afterslip.

607 We find that the steady-state thermal anomaly peaks in the mid-crust at 70–200 °C,  
 608 with contributions from both frictional and viscous shear heating. Our findings for the  
 609 magnitude and spatial distribution of the total thermal anomaly results are broadly con-  
 610 sistent with those of Lambert & Barbot (2016a) and Zhang & Sagiya (2017), who found  
 611 that the total thermal anomaly peaks in the middle of the seismogenic zone at 120 °C  
 612 and 219 °C, respectively. Previous work which included only viscous shear heating pre-  
 613 dict widely differing magnitudes of the expected thermal anomaly, with some predict-  
 614 ing an anomaly on the order of 1–10 °C (Lyzenga et al., 1991; Savage & Lachenbruch,  
 615 2003), essentially negligible, and others predicting an anomaly in the range of 150–200 °C  
 616 (Thatcher & England, 1998; Leloup et al., 1999; Takeuchi & Fialko, 2012; Moore & Par-  
 617 sons, 2015). Our results are most consistent with the latter models. We attribute the  
 618 differences with Lyzenga et al. (1991) to their use of a much weaker viscous flow rheol-  
 619 ogy that placed the BDT around 7 km depth, shallower than in our model, and much  
 620 smaller (by about a factor of 20) heat production at a given stress level. Savage & Lachen-  
 621 bruch (2003) utilized a much smaller friction coefficient, which if set to 0.6 would pro-  
 622 duce a comparable thermal anomaly to ours.

623 Comparison with observations of surface heat flux is one test of the results presented  
 624 here. We find that, for the simulations considered, substantially weakened faults (in our  
 625 simulations, weakening results from elevated pore pressure) are necessary for the pre-  
 626 dicted surface heat flux to be comparable with data from the Parkfield region of the San  
 627 Andreas. This result could be impacted by a number of additional mechanisms and model  
 628 parameter choices. Regional variations in composition, degree of magmatic underplat-  
 629 ing, the passage of the triple junction and slab window, and the opening of a nearby rift  
 630 like in Salton Trough, might lead to differences from our model predictions (e.g., Ful-  
 631 ton & Saffer, 2009; Liu et al., 2012; Han et al., 2016; Neumann et al., 2017; Thatcher

632 & Chapman, 2018). Additionally, dynamic weakening can reduce the background stress  
 633 in the seismogenic zone, reducing the heat generated by frictional shear heating and there-  
 634 fore reducing the thermal anomaly and predicted surface heat flux. Our models suggest  
 635 that a weaker seismogenic zone would also produce lower stresses in the off-fault mate-  
 636 rial, decreasing the heat generated by viscous shear heating as well. It would be straight-  
 637 forward to investigate the effects of dynamic weakening by changing the form of rate-  
 638 and-state friction used here to include flash heating or by extending the model to include  
 639 thermal pressurization (Rice, 2006; Noda et al., 2009; Noda & Lapusta, 2010).

640 Our predictions for the thermal anomaly might ideally be compared with geologic  
 641 indicators of viscous shear heating in exhumed shear zones. Arguably the most compelling  
 642 of these comes from granulite and eclogite facies rocks of the North Davenport shear zone,  
 643 a strike-slip system in dry, strong, continental crust in the Musgrave Block, Australia.  
 644 Camacho et al. (2001) infer a thermal anomaly of  $\sim 200$  °C (in eclogite facies at approx-  
 645 imately 1.2 GPa pressure) in the shear zone relative to the country rock 1 km away. The  
 646 thermal anomaly is inferred by radiometric dating from differences in closure ages dur-  
 647 ing exhumation (with the initially hotter shear zone having a younger closure age than  
 648 the country rock) and a heat conduction model to describe cooling during exhumation.  
 649 This thermal anomaly is larger than predicted by our models at the relevant depths near  
 650 the LAB. We note, however, that they attribute the thermal anomaly to viscous shear  
 651 heating acting over a relatively short time, 0.03 – 0.3 Ma, which is too short for the steady-  
 652 state assumptions made in this paper to apply.

653 Shear heating has also been suggested as an explanation for inverted metamorphic  
 654 sequences around faults (England, 1993). Specifically, some have attributed higher-grade  
 655 metamorphism within fault zones to the thermal anomaly from viscous shear heating (Leloup  
 656 & Kienast, 1993; Leloup et al., 2001). However, it is unclear if shear heating is sufficiently  
 657 large to explain the metamorphism (Gilley et al., 2003), and some alternative geologic  
 658 interpretations suggest that metamorphism preceded the onset of shearing (Searle et al.,  
 659 2010). This subject remains quite controversial (Leloup et al., 2007; Kidder et al., 2013).

## 660 4.2 Fault and Ductile Shear Zone Structure

661 Our results are broadly consistent with observations of the structure of strike-slip  
 662 faults and their ductile roots. However, several assumptions are required to connect our  
 663 simulations to geological structures like mylonite zones. Mylonites are characterized by  
 664 reduced grain size and shear deformation fabrics, produced by dynamic recrystallization  
 665 during viscous flow (Warren & Hirth, 2006; Platt & Behr, 2011). Our simulations pre-  
 666 dict viscous flow, but it is an ongoing effort to add grain size evolution (and grain-size  
 667 sensitive flow laws like diffusion creep) to earthquake sequence simulations (Allison &  
 668 Montesi, 2020). For this discussion, we assume a correspondence between viscous flow  
 669 and mylonite structures. All of our simulations predict a shear zone that is a few kilo-  
 670 meters wide in the lower crust, which is comparable to the width of the exhumed my-  
 671 lonite zone from the middle and lower crust beneath the Alpine Fault (Norris & Cooper,  
 672 2003; Norris & Toy, 2014) and the Salzach–Ennstal–Mariazell–Puchberg Fault (Rosen-  
 673 berg & Schneider, 2008). This is much narrower than the tens of kilometers spanned by  
 674 major exhumed mylonite zones (Bell, 1978; Berthe et al., 1979; Weijermars, 1987; Ca-  
 675 macho et al., 1995; Hanmer, 1988), supporting the hypothesis that these shear zones de-  
 676 veloped beneath a complex of multiple faults (Norris & Cooper, 2003).

677 Our simulations explore the relationship between the down-dip limit of coseismic  
 678 slip in seismogenic earthquakes and the depth of the BDT. Our viscoelastic simulations  
 679 without shear heating, with the exception of those with a 40 km deep LAB (which is shal-  
 680 lower than observed in much of southern California (Lekic et al., 2011)), predict a very  
 681 deep BDT, such that there is no overlap between coseismic slip and appreciable viscous  
 682 flow. This is consistent with our findings in Allison & Dunham (2018) (which use a less

683 mafic composition for the crust), and matches the structure (elastic layer containing a  
 684 fault over a viscoelastic half-space) assumed in related studies (Kato, 2002; Lambert &  
 685 Barbot, 2016a). In contrast, all of our viscoelastic simulations with shear heating pre-  
 686 dict a shallow BDT in the mid-crust, and those with  $\lambda < 0.8$  predict a zone in the mid-  
 687 crust in which coseismic slip and viscous flow both occur. Thus, we find our viscoelas-  
 688 tic simulations with shear heating are consistent with observations of faults which root  
 689 in shear zones in the lower crust (Klosko et al., 1999; Molnar, 1999; Weber et al., 2004;  
 690 Wilson et al., 2004), and many are consistent with observations of zones in which both  
 691 viscous flow and coseismic slip occur (Vissers et al., 1997; Sibson & Toy, 2006; Lin et al.,  
 692 2005; Cole et al., 2007; Griffith et al., 2008; Frost et al., 2011; White, 2012; Kirkpatrick  
 693 & Rowe, 2013).

694 In all our simulations, we held the frictional transition from VW-VS fixed at 16 km  
 695 depth regardless of the background geotherm and thermal anomaly. If instead the VW-  
 696 VS transition was held at 350 °C and allowed to vary in depth and time, the nucleation  
 697 depth and down-dip limit of earthquakes might be controlled by the VW-VS transition  
 698 rather than the BDT for all simulations. On the other hand, recent experimental data  
 699 shows that Westerly granite can remain VW up to at least 600 °C (Mitchell et al., 2016).  
 700 In this case, the BDT would serve as the limit for both earthquake nucleation and down-  
 701 dip coseismic slip.

702 For some faults, such as the San Jacinto, the Newport-Inglewood, and parts of the  
 703 San Andreas, deformation remains highly localized all the way to the Moho (Lemiszki  
 704 & Brown, 1988; Henstock et al., 1997; Zhu, 2000; Vauchez & Tommasi, 2003; Lekic et  
 705 al., 2011; Miller et al., 2014; Inbal et al., 2016). This might indicate that the fault per-  
 706 sists to the mantle (e.g., Shelly, 2010; Inbal et al., 2016) and the BDT occurs below the  
 707 Moho, corresponding perhaps to the behavior predicted by our simulations without shear  
 708 heating and with the coolest geotherms and/or elevated pore pressure. Alternatively, the  
 709 ductile shear zone in the lower crust may be highly localized, a structure which is not  
 710 predicted by any of our simulations. Our model predicts shear zones of about 1–5 km  
 711 width in the lower crust and uppermost mantle, and we find that the width of the shear  
 712 zone changes little with the inclusion of shear heating, consistent with results in Zhang  
 713 & Sagiya (2017), and with scaling arguments in Montési & Zuber (2002), Montési (2013),  
 714 and Moore & Parsons (2015). Significantly localized ductile shear zones would seem to  
 715 require additional weakening mechanisms, such as foliation and fabric development (Bercovici  
 716 & Karato, 2002; Montési, 2013).

## 717 5 Conclusions

718 In conclusion, we have developed a numerical method for simulating earthquake  
 719 cycles with rate-and-state fault friction and off-fault power-law viscoelasticity, account-  
 720 ing for temperature evolution through a fully coupled thermomechanical framework. We  
 721 investigated the interaction between the seismogenic zone, interseismic fault creep, and  
 722 bulk viscous flow in the context of a continental strike-slip fault. We considered a range  
 723 of ambient geotherms, parameterized by the lithosphere-asthenosphere boundary depth,  
 724 hydrostatic or elevated pore fluid pressures along the fault, and frictional shear zone widths  
 725 ranging over two orders of magnitude. We found that the transient temperature changes  
 726 from shear heating can be neglected, and that model results such as the interseismic ther-  
 727 mal anomaly and depth of the BDT are well-characterized by a steady-state approxi-  
 728 mation. Additionally, we find that both frictional and viscous shear heating contributed  
 729 significantly to the total thermal energy of the system, and neither can be neglected.

730 We find that contributions to the thermal anomaly from frictional and viscous shear  
 731 heating are of roughly equal magnitude, though the contribution from viscous shear heat-  
 732 ing is generally deeper and more broadly distributed. Frictional shear heating produces  
 733 transient changes in temperature in the mid-crust in the coseismic and postseismic pe-

734 riod, which for small frictional shear zone widths can reach hundreds of degrees Celsius.  
735 But most results are insensitive to these temperature changes, as a result of the short  
736 lifespan and limited spatial extent of the transient temperature rise. Additionally, fea-  
737 tures like the interseismic thermal anomaly and the depth of the BDT are well-characterized  
738 by a steady-state approximation, in which the effects of earthquake cycles are approx-  
739 imated with time-independent slip velocity and viscous strain rates. And in fact, cycle  
740 simulations which use the steady-state thermal anomaly and neglect transient shear heat-  
741 ing effects all together produce very similar results to those which include the transient  
742 effects, at a significant reduction in computational cost.

## 743 **6 Acknowledgements**

744 This research was supported by the U.S. Geological Survey (G17AP00013), the Na-  
745 tional Science Foundation (EAR-1947448), and the Southern California Earthquake Cen-  
746 ter (Contribution No. 18050). SCEC is funded by NSF Cooperative Agreement EAR-  
747 1600087 & USGS Cooperative Agreement G17AC00047. The source code is available at  
748 <https://bitbucket.org/kallison/scycle>. Simulation data and input files used for this study  
749 can be found at [osf.io/NZMW2/](https://osf.io/NZMW2/).

## Appendix A Spin-up Procedure and Steady-State Solution using a Fixed Point Iteration Method

Earthquake cycle simulations typically must be spun up over many earthquake cycles to achieve system behavior that is independent of the selection of initial conditions (e.g., Takeuchi & Fialko, 2012; Allison & Dunham, 2018). For the parameters considered in this study, the cycle simulations ultimately reach a limit cycle, and all results reported pertain to this spun-up state. Spinning up viscoelastic earthquake cycle simulations with shear heating through brute force time integration is computationally infeasible due to the magnitude of the timescales involved.

There are two timescales relevant to the spin-up process. One is the timescale for the diffusion of heat,

$$T_{\text{th}} = \frac{L^2}{\alpha_{\text{th}}}, \quad (\text{A1})$$

where  $L$  is the maximum length scale of interest, say the seismogenic zone thickness; taking  $L \approx 20$  km we estimate  $T_{\text{th}} \approx 12$  Ma. The second is the Maxwell time,

$$T_{\text{Max}} = \frac{\eta_{\text{eff}}}{\mu}, \quad (\text{A2})$$

which varies by many orders of magnitude with depth, but can be as large as 1 Ma in the lower crust far from the ductile shear zone. These timescales are both so large that it is not computationally feasible to spin the system up through direct simulation of tens of thousands of earthquake cycles, so we have created a fixed point iteration method to solve for steady-state conditions (such as the steady-state shear stress, viscous strain rates, and temperature) which can be used as initial conditions for a cycle simulation. The steady state solution then serves as an initial condition for cycle simulations. This approach considerably shortens the spin-up time needed, though we find that even when starting from the steady-state solution, the cycle simulation must still be integrated through 50-100 earthquake cycles to reach the limit cycle solution in which elastic strain does not increase across successive cycles.

See Supporting Information (Figures S5 and S6) for an comparison between steady-state and cycle-averaged results.

Here we provide more details on the steady state solution method. We define steady state as when the elastic strain rates, and hence stress rates, are zero,

$$\dot{\sigma}_{xy} = 0, \quad \dot{\sigma}_{xz} = 0, \quad (\text{A3})$$

or, equivalently, when viscous strains and particle displacements increase linearly with time,

$$\gamma_{xy} = \dot{\gamma}_{xy}^V t + \gamma_{xy}^{V,0}, \quad (\text{A4})$$

$$\gamma_{xz} = \dot{\gamma}_{xz}^V t + \gamma_{xz}^{V,0}, \quad (\text{A5})$$

$$u = vt + u_0, \quad (\text{A6})$$

where  $\gamma_{xy}^{V,0}$ ,  $\gamma_{xz}^{V,0}$ , and  $u_0$  are the initial viscous strains and displacement, respectively, and  $v = \partial u / \partial t$  is the particle velocity. Combining (A4)-(A6) with Hooke's law (2), produces

$$\sigma_{xy} = \mu \left( \frac{\partial u_0}{\partial y} - \gamma_{xy}^{V,0} \right), \quad \sigma_{xz} = \mu \left( \frac{\partial u_0}{\partial z} - \gamma_{xz}^{V,0} \right). \quad (\text{A7})$$

We set  $u_0 = 0$  without loss of generality, resulting in

$$\sigma_{xy} = -\mu \gamma_{xy}^{V,0}, \quad \sigma_{xz} = -\mu \gamma_{xz}^{V,0}. \quad (\text{A8})$$

Combining Hooke's law (2) and the power-law viscous flow law (3) with Equation (A3) results in

$$\sigma_{xy} = \eta_{\text{eff}} \frac{\partial v}{\partial y}, \quad \sigma_{xz} = \eta_{\text{eff}} \frac{\partial v}{\partial z} \quad (\text{A9})$$

and

$$\dot{\gamma}_{xy} = \frac{\partial v}{\partial y}, \quad \dot{\gamma}_{xz} = \frac{\partial v}{\partial z}. \quad (\text{A10})$$

Using this result, the momentum balance equation (1) can be expressed in terms of  $v$  as

$$\frac{\partial}{\partial y} \left( \eta_{\text{eff}} \frac{\partial v}{\partial y} \right) + \frac{\partial}{\partial z} \left( \eta_{\text{eff}} \frac{\partial v}{\partial z} \right) = 0, \quad (\text{A11})$$

subject to the boundary conditions

$$\sigma_{xy}(0, z) = \eta_{\text{eff}} \frac{\partial v}{\partial y} \Big|_{y=0} = \tau_{ss}, \quad (\text{A12})$$

$$v(L_y, z) = V_L/2, \quad (\text{A13})$$

$$\sigma_{xz}(y, 0) = \eta_{\text{eff}} \frac{\partial v}{\partial z} \Big|_{z=0} = 0, \quad (\text{A14})$$

$$\sigma_{xz}(y, L_z) = \eta_{\text{eff}} \frac{\partial v}{\partial z} \Big|_{z=L_z} = 0, \quad (\text{A15})$$

where  $\tau_{ss}(V)$  is the steady-state shear stress on the fault.

We assume steady-state friction to evaluate  $\tau_{ss}(V)$ , but note that the steady-state slip velocity  $V$  is not necessarily equal to the loading velocity  $V_L$  (because viscous strain can also accommodate tectonic displacement), and must be determined as part of the solution to the steady-state problem. This formulation neglects the transient effects of earthquakes, providing an approximation to the cycle-averaged frictional strength of the fault. See Supplemental Information (Figure S6) for an illustration of this approximation. To solve for  $\tau_{ss}$ , we use the method described in Allison & Dunham (2018) to integrate Equations (1)-(4) (the viscoelastic momentum balance equation), (11)-(10) (boundary conditions), and the rate-and-state expression for  $\tau_{ss}(V)$  until  $\tau_{ss}(V)$  and  $V$  cease to change appreciably.

Given  $\tau_{ss}(V)$ , Equations (A9)-(A15) are a nonlinear set of equations for the steady-state effective viscosity, stresses, viscous strains, and viscous strain rates. We solve these equations using a fixed point iteration method, illustrated in the green box in Figure A1. First guess an initial effective viscosity  $\eta_{\text{eff}}^i$ , and use it to solve Equations (A9)-(A15). Then compute a new effective viscosity  $\eta_{\text{eff}}$  using Equation (4). Finally, compute an update for effective viscosity

$$\eta_{\text{eff}}^{i+1} = \alpha \eta_{\text{eff}} + (1 - \alpha) \eta_{\text{eff}}^i, \quad (\text{A16})$$

where  $\alpha$  is a damping factor, and  $0 < \alpha \leq 1$ . If  $\alpha$  is too large, the fixed point method may not converge to a steady-state effective viscosity. We find that  $\alpha = 0.2$  works well for the parameters considered in this paper. We also find that Equations (A11)-(A15) produce a poorly conditioned linear system, due to the wide range of values taken by  $\eta_{\text{eff}}$ , spanning many orders of magnitude. To remedy this, we impose a ceiling on the effective viscosity,  $\eta_{\text{max}} = 10^{26}$  Pa s, using the harmonic average

$$\eta_{\text{eff}}^{-1} = \eta_{\text{dis}}^{-1} + \eta_{\text{max}}^{-1}, \quad (\text{A17})$$

where  $\eta_{\text{dis}}$  is the effective viscosity resulting from dislocation creep in Equation (4). We find that varying  $\eta_{\text{max}}$  over 3 orders of magnitude does not change our results for the steady-state shear stress on the fault and its deep extension, nor the steady-state thermal anomaly.

Given the steady-state shear stress and effective viscosity, the steady-state temperature perturbation can be computed from

$$\frac{\partial}{\partial y} \left( k \frac{\partial \Delta T_{ss}}{\partial y} \right) + \frac{\partial}{\partial z} \left( k \frac{\partial \Delta T_{ss}}{\partial z} \right) + Q_{\text{visc}} + Q_{\text{fric}} = 0 \quad (\text{A18})$$

839 with the previously stated boundary conditions. We also use a damping factor  $\beta$  to up-  
 840 date the temperature perturbation

$$841 \quad \Delta T_{ss}^{j+1} = \beta \Delta T_{ss} + (1 - \beta) \Delta T_{ss}^j. \quad (\text{A19})$$

842 We find that convergence of the overall fixed point system is more sensitive to  $\beta$  than  
 843  $\alpha$ , and use  $\beta = 0.15$ .

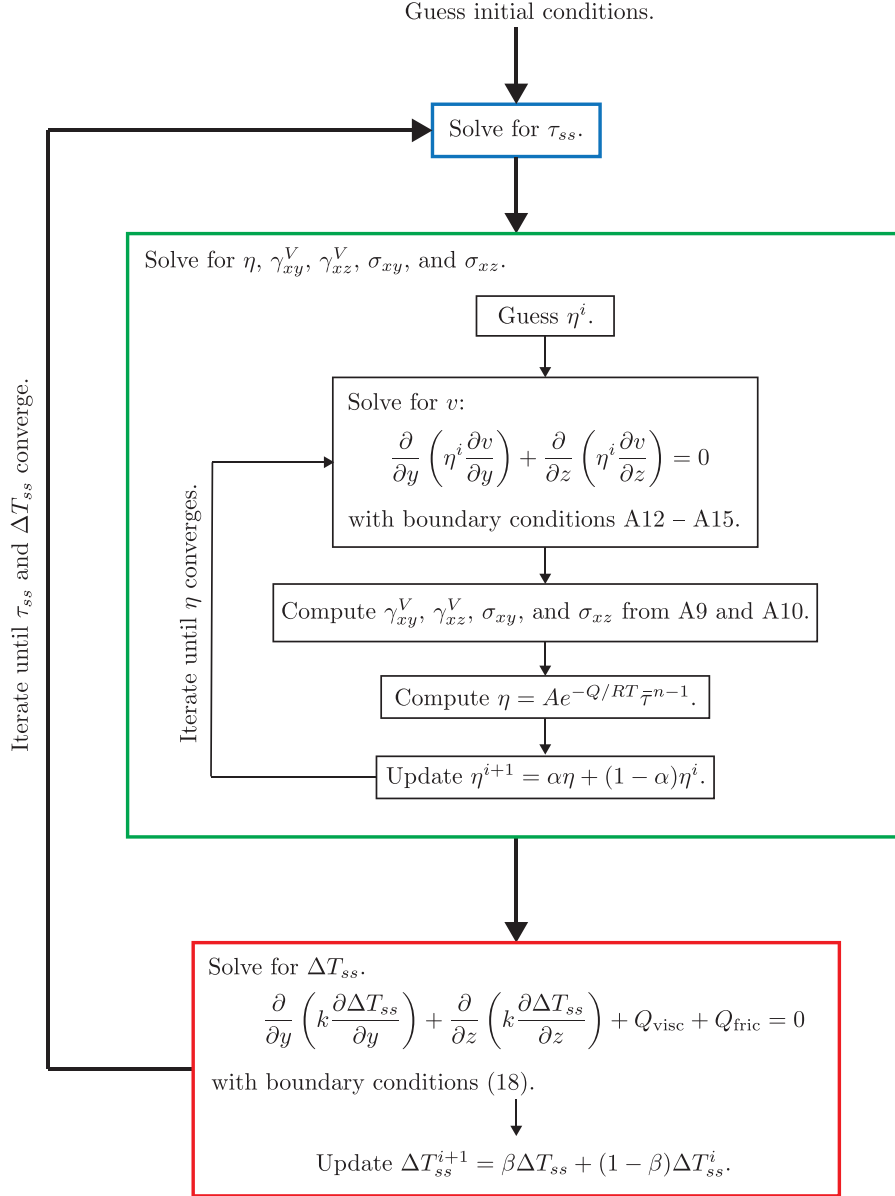


**Figure A1.** Illustration of the fixed point iteration method used to compute the steady-state solution.

## 844 References

845 Aagaard, B. T., Knepley, M. G., & Williams, C. A. (2013). A domain decomposi-

- 846 tion approach to implementing fault slip in finite-element models of quasi-static  
847 and dynamic crustal deformation. *Journal of Geophysical Research: Solid Earth*,  
848 *118*(6), 3059–3079. Retrieved from <http://doi.wiley.com/10.1002/jgrb.50217>  
849 doi: 10.1002/jgrb.50217
- 850 Aharonov, E., & Scholz, C. H. (2018). A Physics-Based Rock Friction Constitutive  
851 Law: Steady State Friction. *Journal of Geophysical Research: Solid Earth*, *123*(2),  
852 1591–1614. doi: 10.1002/2016JB013829
- 853 Aharonov, E., & Scholz, C. H. (2019). The Brittle-Ductile Transition Predicted  
854 by a Physics-Based Friction Law. *Journal of Geophysical Research: Solid Earth*,  
855 *124*(3), 2721–2737. doi: 10.1029/2018JB016878
- 856 Allison, K. L., & Dunham, E. M. (2018). *Earthquake cycle simulations with*  
857 *rate-and-state friction and power-law viscoelasticity* (Vol. 733). doi: 10.1016/  
858 j.tecto.2017.10.021
- 859 Allison, K. L., & Montesi, L. G. (2020). *Three definitions of ductile shear zones*  
860 *resulting from grain-size evolution below a frictional fault — Southern Califor-*  
861 *nia Earthquake Center*. Retrieved from [https://www.scec.org/publication/](https://www.scec.org/publication/10222)  
862 [10222](https://www.scec.org/publication/10222)
- 863 Andrews, D. J. (2002). A fault constitutive relation accounting for thermal pressur-  
864 ization of pore fluid. *Journal of Geophysical Research: Solid Earth*, *107*(B12),  
865 ESE 15–1–ESE 15–8. Retrieved from [http://doi.wiley.com/10.1029/](http://doi.wiley.com/10.1029/2002JB001942)  
866 [2002JB001942](http://doi.wiley.com/10.1029/2002JB001942) doi: 10.1029/2002JB001942
- 867 Barbot, S. D., & Fialko, Y. (2010). A unified continuum representation of post-  
868 seismic relaxation mechanisms: Semi-analytic models of afterslip, poroelastic  
869 rebound and viscoelastic flow. *Geophysical Journal International*, *182*(3), 1124–  
870 1140. doi: 10.1111/j.1365-246X.2010.04678.x
- 871 Barbot, S. D., Lapusta, N., & Avouac, J.-P. (2012). Under the hood of the  
872 earthquake machine: Toward predictive modeling of the seismic cycle. *Science*,  
873 *336*(May), 707–710. doi: 10.1126/science.1218796
- 874 Beeler, N. M., Hirth, G., Tullis, T. E., & Webb, C. H. (2018). On the depth extent  
875 of coseismic rupture. *Bulletin of the Seismological Society of America*, *108*(2),  
876 761–780. Retrieved from [https://pubs.geoscienceworld.org/ssa/bssa/](https://pubs.geoscienceworld.org/ssa/bssa/article/108/2/761/528132/On-the-Depth-Extent-of-Coseismic-RuptureOn-thehttps://pubs.geoscienceworld.org/ssa/bssa/article/528132/On-the-Depth-Extent-of-Coseismic-RuptureOn-the)  
877 [article/108/2/761/528132/On-the-Depth-Extent-of-Coseismic-RuptureOn-](https://pubs.geoscienceworld.org/ssa/bssa/article/108/2/761/528132/On-the-Depth-Extent-of-Coseismic-RuptureOn-thehttps://pubs.geoscienceworld.org/ssa/bssa/article/528132/On-the-Depth-Extent-of-Coseismic-RuptureOn-the)  
878 [thehttps://pubs.geoscienceworld.org/ssa/bssa/article/528132/On-the](https://pubs.geoscienceworld.org/ssa/bssa/article/528132/On-the-Depth-Extent-of-Coseismic-RuptureOn-the)  
879 [-Depth-Extent-of-Coseismic-RuptureOn-the](https://pubs.geoscienceworld.org/ssa/bssa/article/528132/On-the-Depth-Extent-of-Coseismic-RuptureOn-the) doi: 10.1785/0120160295
- 880 Behr, W. M., & Hirth, G. (2014). Rheological properties of the mantle lid beneath  
881 the Mojave region in southern California. *Earth and Planetary Science Letters*,  
882 *393*, 60–72. doi: 10.1016/j.epsl.2014.02.039
- 883 Behr, W. M., & Platt, J. P. (2014). Brittle faults are weak, yet the ductile middle  
884 crust is strong: Implications for lithospheric mechanics. *Geophysical Research*  
885 *Letters*, *41*(22), 8067–8075. Retrieved from [http://doi.wiley.com/10.1002/](http://doi.wiley.com/10.1002/2014GL061349)  
886 [2014GL061349](http://doi.wiley.com/10.1002/2014GL061349)[http://onlinelibrary.wiley.com/doi/10.1002/2014GL061349/](http://onlinelibrary.wiley.com/doi/10.1002/2014GL061349/pdf)  
887 [pdf](http://onlinelibrary.wiley.com/doi/10.1002/2014GL061349/pdf) doi: 10.1002/2014GL061349
- 888 Bell, T. H. (1978). Progressive deformation and reorientation of fold axes  
889 in a ductile mylonite zone: the Woodroffe Thrust. *Tectonophysics*, *44*,  
890 285–320. Retrieved from [https://ac-els-cdn-com.stanford.idm.oclc](https://ac-els-cdn-com.stanford.idm.oclc.org/0040195178900744/1-s2.0-0040195178900744-main.pdf?{\_}tid=3d79be56-c57b-4204-b779-bc24962d5605{\&}acdnat=1533234414{\_}2430183e14bb61e8b2192712b56fc1d4)  
891 [.org/0040195178900744/1-s2.0-0040195178900744-main.pdf?{\\\_}tid=](https://ac-els-cdn-com.stanford.idm.oclc.org/0040195178900744/1-s2.0-0040195178900744-main.pdf?{\_}tid=3d79be56-c57b-4204-b779-bc24962d5605{\&}acdnat=1533234414{\_}2430183e14bb61e8b2192712b56fc1d4)  
892 [3d79be56-c57b-4204-b779-bc24962d5605{\&}acdnat=1533234414{\\\_}](https://ac-els-cdn-com.stanford.idm.oclc.org/0040195178900744/1-s2.0-0040195178900744-main.pdf?{\_}tid=3d79be56-c57b-4204-b779-bc24962d5605{\&}acdnat=1533234414{\_}2430183e14bb61e8b2192712b56fc1d4)  
893 [\\_}2430183e14bb61e8b2192712b56fc1d4](https://ac-els-cdn-com.stanford.idm.oclc.org/0040195178900744/1-s2.0-0040195178900744-main.pdf?{\_}tid=3d79be56-c57b-4204-b779-bc24962d5605{\&}acdnat=1533234414{\_}2430183e14bb61e8b2192712b56fc1d4)
- 894 Bercovici, D., & Karato, S.-i. (2002). Theoretical Analysis of Shear Localization  
895 in the Lithosphere. *Reviews in Mineralogy and Geochemistry*, *51*(1), 387–420.  
896 Retrieved from [https://pubs.geoscienceworld.org/rimg/article/51/1/](https://pubs.geoscienceworld.org/rimg/article/51/1/387-420/87454)  
897 [387-420/87454](https://pubs.geoscienceworld.org/rimg/article/51/1/387-420/87454) doi: 10.2138/gsrmg.51.1.387
- 898 Berthe, D., Choukroune, P., Jegouze, P., & Jegouze, P. (1979). Orthogneiss,  
899 mylonite and non coaxial deformation of granites: the example of the

- 900 South Armorican Shear Zone. *Journal of Structural Geology*, 1(1), 31–  
 901 42. Retrieved from [https://ac-els-cdn-com.stanford.idm.oclc.org/  
 902 0191814179900191/1-s2.0-0191814179900191-main.pdf?{\\\_}tid=  
 903 511706f1-2524-4578-9ffd-ed21d02d1563{\&}acdnat=1533210211{\\\_}  
 904 \\_}c311d344a1c796706105bb67b50db1a1](https://ac-els-cdn-com.stanford.idm.oclc.org/0191814179900191/1-s2.0-0191814179900191-main.pdf?{\_}tid=511706f1-2524-4578-9ffd-ed21d02d1563{\&}acdnat=1533210211{\_}c311d344a1c796706105bb67b50db1a1)
- 905 Blanpied, M. L., Lockner, D. A., & Byerlee, J. D. (1991). Fault stability inferred  
 906 from granite sliding experiments at hydrothermal conditions. *Geophysical Re-  
 907 search Letters*, 18(4), 609–612. Retrieved from [http://doi.wiley.com/10.1029/  
 908 91GL00469](http://doi.wiley.com/10.1029/91GL00469) doi: 10.1029/91GL00469
- 909 Blanpied, M. L., Lockner, D. A., & Byerlee, J. D. (1995). Frictional slip of granite at  
 910 hydrothermal conditions. *Journal of Geophysical Research: Solid Earth*, 100(B7).  
 911 doi: 10.1029/95JB00862
- 912 Brace, W. F., & Kohlstedt, D. L. (1980). Limits on lithospheric stress imposed  
 913 by laboratory experiments. *Journal of Geophysical Research*, 85(B11), 6248–  
 914 6252. Retrieved from <http://doi.wiley.com/10.1029/JB085iB11p06248> doi:  
 915 10.1029/JB085iB11p06248
- 916 Bürgmann, R., & Dresen, G. (2008). Rheology of the lower crust and upper mantle:  
 917 Evidence from rock mechanics, geodesy, and field observations. *Annual Review  
 918 of Earth and Planetary Sciences*, 36(1), 531–567. Retrieved from [http://www  
 919 .annualreviews.org/doi/10.1146/annurev.earth.36.031207.124326http://  
 920 www.annualreviews.org/doi/abs/10.1146/annurev.earth.36.031207.124326  
 921 doi: 10.1146/annurev.earth.36.031207.124326](http://www.annualreviews.org/doi/10.1146/annurev.earth.36.031207.124326http://www.annualreviews.org/doi/abs/10.1146/annurev.earth.36.031207.124326)
- 922 Byerlee, J. (1978). Friction of rocks. *Pure and Applied Geophysics*, 116(4-5), 615–  
 923 626. Retrieved from <http://link.springer.com/10.1007/BF00876528> doi: 10  
 924 .1007/BF00876528
- 925 Byerlee, J. (1990). Friction, overpressure and fault normal compression. *Geophysi-  
 926 cal Research Letters*, 17(12), 2109–2112. Retrieved from [http://doi.wiley.com/  
 927 10.1029/GL017i012p02109](http://doi.wiley.com/10.1029/GL017i012p02109) doi: 10.1029/GL017i012p02109
- 928 Camacho, A., McDougall, I., Armstrong, R., & Braun, J. (2001). Evidence for shear  
 929 heating, Musgrave Block, central Australia. *Journal of Structural Geology*, 23(6-  
 930 7), 1007–1013. doi: 10.1016/S0191-8141(00)00172-3
- 931 Camacho, A., Vernon, R. H., & Fitz Gerald, J. D. (1995). Large vol-  
 932 umes of anhydrous pseudotachylyte in the Woodroffe Thrust, eastern Mus-  
 933 grave Ranges, Australia. *Journal of Structural Geology*, 17(3), 371 –  
 934 383. Retrieved from [https://ac-els-cdn-com.stanford.idm.oclc.org/  
 935 019181419400069C/1-s2.0-019181419400069C-main.pdf?{\\\_}tid=  
 936 057c512d-c053-4761-a44b-28e5f82ad3aa{\&}acdnat=1533233965{\\\_}  
 937 \\_}33d67765530637efee4eb385303ec6d1](https://ac-els-cdn-com.stanford.idm.oclc.org/019181419400069C/1-s2.0-019181419400069C-main.pdf?{\_}tid=057c512d-c053-4761-a44b-28e5f82ad3aa{\&}acdnat=1533233965{\_}33d67765530637efee4eb385303ec6d1)
- 938 Cattania, C. (2019). Complex Earthquake Sequences On Simple Faults. *Geophysical  
 939 Research Letters*, 46(17-18), 10384–10393. doi: 10.1029/2019GL083628
- 940 Chatzaras, V., Tikoff, B., Newman, J., Withers, A. C., & Drury, M. R. (2015). Man-  
 941 tle strength of the San Andreas fault system and the role of mantle-crust feed-  
 942 backs. *Geology*, 43(10), 891–894. Retrieved from [http://geology.gsapubs.org/  
 943 lookup/doi/10.1130/G36752.1](http://geology.gsapubs.org/lookup/doi/10.1130/G36752.1) doi: 10.1130/G36752.1
- 944 Chester, F. M. (1995). A rheologic model for wet crust applied to strike slip faults.  
 945 *Journal of Geophysical Research-Solid Earth*, 100(B7), 13033–13044. Retrieved  
 946 from <http://doi.wiley.com/10.1029/95JB00313> doi: 10.1029/95JB00313
- 947 Chester, F. M., & Chester, J. S. (1998). Ultracataclasite structure and friction pro-  
 948 cesses of the Punchbowl Fault, San Andreas system, California. *Tectonophysics*,  
 949 295(1), 199–221. Retrieved from [http://www.sciencedirect.com/science/  
 950 article/pii/S0040195198001218](http://www.sciencedirect.com/science/article/pii/S0040195198001218) doi: 10.1016/S0040-1951(98)00121-8
- 951 Chester, F. M., Chester, J. S., Kirschner, D. L., Schulz, S. E., & Evans, J. P. (2004).  
 952 Structure of large-displacement, strike-slip fault zones in the brittle continental  
 953 crust. In G. D. Karner, B. Taylor, N. W. Driscoll, & D. L. Kohlstedt (Eds.), *Rhe-*

- 954 *ology and deformation in the lithosphere at continental margins* (pp. 223 – 260).  
 955 New York: Columbia University Press.
- 956 Cole, J., Hacker, B., Ratschbacher, L., Dolan, J., Seward, G., Frost, E., & Frank, W.  
 957 (2007). Localized ductile shear below the seismogenic zone: Structural analysis  
 958 of an exhumed strike-slip fault, Austrian Alps. *Journal of Geophysical Research*,  
 959 *112*(B12). Retrieved from <http://doi.wiley.com/10.1029/2007JB004975> doi:  
 960 10.1029/2007JB004975
- 961 Dieterich, J. H. (1978). Time-dependent friction and the mechanics of stick-  
 962 slip. *Pure and Applied Geophysics*, *116*(4-5), 790–806. Retrieved from  
 963 <http://link.springer.com/10.1007/BF00876539> doi: 10.1007/BF00876539
- 964 Dieterich, J. H. (1979). Modeling of rock friction 1. Experimental results and con-  
 965 stitutive equations. *Journal of Geophysical Research: Solid Earth*, *84*(B5), 2161–  
 966 2168. Retrieved from <http://doi.wiley.com/10.1029/JB084iB05p02161> doi:  
 967 10.1029/JB084iB05p02161
- 968 Duru, K., Allison, K. L., Rivet, M., & Dunham, E. M. (2019). Dynamic rupture and  
 969 earthquake sequence simulations using the wave equation in second-order form.  
 970 *Geophysical Journal International*, *219*(2), 796–815. doi: 10.1093/gji/ggz319
- 971 England, P. (1993). The Interpretation of inverted metamorphic isograds using sim-  
 972 ple physical calculations. *Tectonics*, *12*(1), 145–157.
- 973 Erickson, B. A., & Dunham, E. M. (2014). An efficient numerical method for earth-  
 974 quake cycles in heterogeneous media: Alternating subbasin and surface-rupturing  
 975 events on faults crossing a sedimentary basin. *Journal of Geophysical Research:*  
 976 *Solid Earth*, *119*(4), 3290–3316. Retrieved from [http://doi.wiley.com/](http://doi.wiley.com/10.1002/2013JB010614)  
 977 [10.1002/2013JB010614](http://doi.wiley.com/10.1002/2013JB010614) doi: 10.1002/2013JB010614
- 978 Erickson, B. A., Jiang, J., Barall, M., Lapusta, N., Dunham, E. M., Harris, R., ...  
 979 Wei, M. (2020). The Community Code Verification Exercise for Simulating Se-  
 980 quences of Earthquakes and Aseismic Slip (SEAS). *Seismological Research Letters*,  
 981 *91*(2A), 1–40. doi: 10.1785/0220190248
- 982 Freed, A. M., & Bürgmann, R. (2004). Evidence of power-law flow in the Mojave  
 983 desert mantle. *Nature*, *430*, 548–551.
- 984 Frost, E., Dolan, J., Ratschbacher, L., Hacker, B., & Seward, G. (2011). Direct ob-  
 985 servation of fault zone structure at the brittle-ductile transition along the Salzach-  
 986 Ennstal-Mariazell-Puchberg fault system, Austrian Alps. *Journal of Geophysical*  
 987 *Research: Solid Earth*, *116*(2). Retrieved from [http://doi.wiley.com/10.1029/](http://doi.wiley.com/10.1029/2010JB007719)  
 988 [2010JB007719](http://doi.wiley.com/10.1029/2010JB007719) doi: 10.1029/2010JB007719
- 989 Fulton, P. M., & Saffer, D. M. (2009). Potential role of mantle-derived fluids in  
 990 weakening the San Andreas Fault. *Journal of Geophysical Research: Solid Earth*,  
 991 *114*(7), 1–15. doi: 10.1029/2008JB006087
- 992 Fulton, P. M., Saffer, D. M., Harris, R. N., & Bekins, B. A. (2004). Re-  
 993 evaluation of heat flow data near Parkfield, CA: Evidence for a weak San An-  
 994 dreas Fault. *Geophysical Research Letters*, *31*(15), L15S15. Retrieved from  
 995 <http://doi.wiley.com/10.1029/2003GL019378> doi: 10.1029/2003GL019378
- 996 Gilley, L. D., Harrison, T. M., Leloup, P. H., Ryerson, F. J., Lovera, O. M., &  
 997 Wang, J.-H. (2003). Direct dating of left-lateral deformation along the Red  
 998 River shear zone, China and Vietnam. *Journal of Geophysical Research: Solid*  
 999 *Earth*, *108*(B2). doi: 10.1029/2001jb001726
- 1000 Goetze, C., & Evans, B. (1979). Stress and temperature in the bending litho-  
 1001 sphere as constrained by experimental rock mechanics. *Geophysical Journal*  
 1002 *International*, *59*(3), 463–478. Retrieved from [https://academic.oup.com/](https://academic.oup.com/gji/article-lookup/doi/10.1111/j.1365-246X.1979.tb02567.x)  
 1003 [gji/article-lookup/doi/10.1111/j.1365-246X.1979.tb02567.x](https://academic.oup.com/gji/article-lookup/doi/10.1111/j.1365-246X.1979.tb02567.x)[http://](http://gji.oxfordjournals.org/content/59/3/463.short)  
 1004 [gji.oxfordjournals.org/content/59/3/463.short](http://gji.oxfordjournals.org/content/59/3/463.short) doi: 10.1111/j.1365-246X  
 1005 .1979.tb02567.x
- 1006 Griffith, W. A., Di Toro, G., Pennacchioni, G., & Pollard, D. D. (2008). Thin  
 1007 pseudotachylytes in faults of the Mt. Abbot quadrangle, Sierra Nevada: Physical

- constraints for small seismic slip events. *Journal of Structural Geology*, 30(9), 1086–1094. doi: 10.1016/j.jsg.2008.05.003
- Han, L., Hole, J. A., Stock, J. M., Fuis, G. S., Kell, A., Driscoll, N. W., ... Lázaro-Mancilla, O. (2016). Continental rupture and the creation of new crust in the Salton Trough rift, Southern California and northern Mexico: Results from the Salton Seismic Imaging Project. *Journal of Geophysical Research: Solid Earth*, 121(10), 7469–7489. doi: 10.1002/2016JB013139
- Hanmer, S. (1988). Great Slave Lake Shear Zone, Canadian Shield: reconstructed vertical profile of a crustal-scale fault zone. *Tectonophysics*, 149(3-4), 245–264. doi: 10.1016/0040-1951(88)90176-X
- Henstock, T. J., Levander, A., & Hole, J. A. (1997). Deformation in the lower crust of the San Andreas Fault System in Northern California. *Science*, 278(5338), 650–653. Retrieved from <http://www.sciencemag.org/cgi/doi/10.1126/science.278.5338.650><http://www.sciencemag.org/content/278/5338/650.abstract><http://www.sciencemag.org/content/278/5338/650.full.pdf> doi: 10.1126/science.278.5338.650
- Hirth, G., & Kohlstedt, D. L. (2003). Rheology of the upper mantle and the mantle wedge: A view from the experimentalists. *Geophysical Monograph Series*, 138, 83–105. doi: 10.1029/138GM06
- Hu, J., & Sun, Q. (2020). The effect of high temperature and pressure on rock friction coefficient: a review. *International Journal of Earth Sciences*, 1–11.
- Hubbert, M. K., & Rubey, W. W. (1959). Role of fluid pressure in mechanics of overthrust faulting. *Bulletin of the Geological Society of America*, 70, 115–166. Retrieved from <https://pubs.geoscienceworld.org/gsa/gsabulletin/article-pdf/70/2/115/3416670/i0016-7606-70-2-115.pdf>
- Humphreys, E. D., & Hager, B. (1990). A kinematic model for the late Cenozoic development of southern California crust and upper mantle. *Journal of Geophysical Research-Solid Earth*, 95(B12), 19747. Retrieved from <http://doi.wiley.com/10.1029/JB095iB12p19747><http://publication.livfe.id/139152> doi: 10.1029/JB095iB12p19747
- Inbal, A., Ampuero, J. P., & Clayton, R. W. (2016). Localized seismic deformation in the upper mantle revealed by dense seismic arrays. *Science*, 354(6308), 88–93. Retrieved from <http://science.sciencemag.org/content/354/6308/88/tab-pdf> doi: 10.1126/science.aaf1370
- Jackson, J. (2002). Strength of the continental lithosphere: Time to abandon the jelly sandwich? *GSA Today*, 12(9), 4–10. doi: 10.1130/1052-5173(2002)012<0004:SOTCLT>2.0.CO;2
- Jackson, J., McKenzie, D., Priestley, K., & Emmerson, B. (2008). New views on the structure and rheology of the lithosphere. *Journal of the Geological Society*, 165(2), 453–465. doi: 10.1144/0016-76492007-109
- Johnson, K. M., Hilley, G. E., & Bürgmann, R. (2007). Influence of lithosphere viscosity structure on estimates of fault slip rate in the Mojave region of the San Andreas Fault system. *Journal of Geophysical Research: Solid Earth*, 112(7). Retrieved from <http://doi.wiley.com/10.1029/2006JB004842> doi: 10.1029/2006JB004842
- Kaneko, Y., Ampuero, J. P., & Lapusta, N. (2011). Spectral-element simulations of long-term fault slip: Effect of low-rigidity layers on earthquake-cycle dynamics. *Journal of Geophysical Research: Solid Earth*, 116(10). Retrieved from <http://doi.wiley.com/10.1029/2011JB008395> doi: 10.1029/2011JB008395
- Kato, N. (2002). Seismic cycle on a strike-slip fault with rate- and state-dependent strength in an elastic layer overlying a viscoelastic half-space. *Earth, Planets and Space*, 54(11), 1077–1083. Retrieved from <http://earth-planets-space.springeropen.com/articles/10.1186/BF03353305> doi: 10.1186/BF03353305
- Kidder, S. B., Herman, F., Saleeby, J., Avouac, J. P., Ducea, M. N., & Chapman,

- 1062 A. (2013). Shear heating not a cause of inverted metamorphism. *Geology*, *41*(8),  
1063 899–902. doi: 10.1130/G34289.1
- 1064 Kirkpatrick, J. D., & Rowe, C. D. (2013). Disappearing ink: How pseudotachylytes  
1065 are lost from the rock record. *Journal of Structural Geology*, *52*(1), 183–198. doi:  
1066 10.1016/j.jsg.2013.03.003
- 1067 Klosko, E. R., Wu, F. T., Anderson, H. J., Eberhart-Phillips, D., McEvelly,  
1068 T. V., Audoiné, E., ... Gledhill, K. R. (1999). Upper mantle anisotropy  
1069 in the New Zealand region. *Geophysical Research Letters*, *26*(10), 1497 –  
1070 1500. Retrieved from <http://doi.wiley.com/10.1029/1999GL900273>:  
1071 `{\%}5CUsers{\%}5CYifan{\%}5CDocuments{\%}5CReadCubeMedia{\%`  
1072 `}5CGeophysicalResearchLetters1999KloskoE.pdf{\%}5Cnhttp://dx.doi.org/  
1073 10.1029/1999GL900273https://s3.amazonaws.com/objects.readcube.com/  
1074 articles/downloaded/wiley/4b` doi: 10.1029/1999GL900273
- 1075 Lachenbruch, A. H., & Sass, J. H. (1977). Heat flow in the United States and the  
1076 thermal regime of the crust. In J. Heacock, G. V. Keller, O. E., & G. Simmons  
1077 (Eds.), *In the earth's crust*. American Geophysical Union (AGU). Retrieved from  
1078 <http://doi.wiley.com/10.1029/GM020p0626> doi: 10.1029/GM020p0626
- 1079 Lachenbruch, A. H., Sass, J. H., & Galanis, S. P. (1985). Heat flow in southern-  
1080 most California and the origin of the Salton Trough. *Journal of Geophysical Re-*  
1081 *search*, *90*(B8), 6709 – 6736. Retrieved from [http://doi.wiley.com/10.1029/  
1082 JB090iB08p06709](http://doi.wiley.com/10.1029/JB090iB08p06709) doi: 10.1029/JB090iB08p06709
- 1083 Lambert, V., & Barbot, S. (2016b). The role of thermal processes in defining the  
1084 seismogenic zone: The interplay between faults and shear zones. *American Geo-*  
1085 *physical Union, Fall General Assembly 2016, abstract id. T22B-03*. Retrieved  
1086 from <http://adsabs.harvard.edu/abs/2016AGUFM.T22B..03L>
- 1087 Lambert, V., & Barbot, S. D. (2016a). Contribution of viscoelastic flow in earth-  
1088 quake cycles within the lithosphere-asthenosphere system. *Geophysical Research*  
1089 *Letters*, *43*(19), 10,142–10,154. Retrieved from [http://doi.wiley.com/10.1002/  
1090 2016GL070345](http://doi.wiley.com/10.1002/2016GL070345) doi: 10.1002/2016GL070345.1
- 1091 Lapusta, N., & Rice, J. R. (2003a). Low-heat and low-stress fault operation in  
1092 earthquake models of statically strong but dynamically weak faults. *American*  
1093 *Geophysical Union, Fall Meeting 2003, abstract id. S51B-02*. Retrieved from  
1094 <http://adsabs.harvard.edu/abs/2003AGUFM.S51B..02L>
- 1095 Lapusta, N., & Rice, J. R. (2003b). Nucleation and early seismic propagation of  
1096 small and large events in a crustal earthquake model. *Journal of Geophysical Re-*  
1097 *search: Solid Earth*, *108*(B4). Retrieved from [http://doi.wiley.com/10.1029/  
1098 2001JB000793](http://doi.wiley.com/10.1029/2001JB000793) doi: 10.1029/2001JB000793
- 1099 Lapusta, N., Rice, J. R., Ben-Zion, Y., & Zheng, G. (2000). Elastodynamic anal-  
1100 ysis for slow tectonic loading with spontaneous rupture episodes on faults with  
1101 rate- and state-dependent friction. *Journal of Geophysical Research: Solid Earth*,  
1102 *105*(B10), 23765–23789. Retrieved from [http://doi.wiley.com/10.1029/  
1103 2000JB900250](http://doi.wiley.com/10.1029/2000JB900250) doi: 10.1029/2000JB900250
- 1104 Lekic, V., French, S. W., & Fisher, K. M. (2011). Lithospheric thinning beneath  
1105 rifted regions of southern California. *Science*, *334*, 783 – 787.
- 1106 Leloup, P., Arnaud, N., Lacassin, R., Kienast, J. R., Harrison, T., Phan Trong,  
1107 T. T., ... Tapponnier, P. (2001). New constraints on the structure, ther-  
1108 mochronology, and timing of the Ailao Shan-Red River shear zone, SE Asia.  
1109 *Journal of Geophysical Research: Solid Earth*, *106*(B4), 6683–6732. doi:  
1110 10.1029/2000jb900322
- 1111 Leloup, P., & Kienast, J. R. (1993). High-temperature metamorphism in  
1112 a major strike-slip shear zone: the Ailao Shan-Red River, People's Repub-  
1113 lic of China. *Earth and Planetary Science Letters*, *118*(1-4), 213–234. doi:  
1114 10.1016/0012-821X(93)90169-A
- 1115 Leloup, P., Ricard, Y., Battaglia, J., & Lacassin, R. (1999). Shear heating in con-

- 1116 tinal strike-slip shear zones: Model and field examples. *Geophysical Journal*  
 1117 *International*, 136(1), 19–40. Retrieved from [https://academic.oup.com/](https://academic.oup.com/gji/article-lookup/doi/10.1046/j.1365-246X.1999.00683.x)  
 1118 [gji/article-lookup/doi/10.1046/j.1365-246X.1999.00683.x](https://academic.oup.com/gji/article-lookup/doi/10.1046/j.1365-246X.1999.00683.x) doi:  
 1119 10.1046/j.1365-246X.1999.00683.x
- 1120 Leloup, P., Tapponnier, P., Lacassin, R., & Searle, M. (2007). Discussion on the  
 1121 role of the Red River shear zone, Yunnan and Vietnam, in the continental ex-  
 1122 trusion of SE Asia *Journal*, Vol. 163, 2006, 1025–1036. *Journal of the Geolog-*  
 1123 *ical Society*, 164(6), 1253–1260. Retrieved from [https://doi.org/10.1144/](https://doi.org/10.1144/0016-76492007-065)  
 1124 [0016-76492007-065](https://doi.org/10.1144/0016-76492007-065) doi: 10.1144/0016-76492007-065
- 1125 Lemiszki, P. J., & Brown, L. D. (1988). Variable crustal structure of strike-slip fault  
 1126 zones as observed on deep seismic reflection profiles. *Bulletin of the Geological So-*  
 1127 *ciety of America*, 100(5), 665–676. Retrieved from [http://gsabulletin.gsapubs](http://gsabulletin.gsapubs.org/cgi/doi/10.1130/0016-7606(1988)100{\\%}3C0665:VCSOSS{\\%}3E2.3.CO;2)  
 1128 [.org/cgi/doi/10.1130/0016-7606\(1988\)100{\\%}3C0665:VCSOSS{\\%}3E2.3.CO;](http://gsabulletin.gsapubs.org/cgi/doi/10.1130/0016-7606(1988)100{\\%}3C0665:VCSOSS{\\%}3E2.3.CO;2)  
 1129 [2](http://gsabulletin.gsapubs.org/cgi/doi/10.1130/0016-7606(1988)100{\\%}3C0665:VCSOSS{\\%}3E2.3.CO;2) doi: 10.1130/0016-7606(1988)100(0665:VCSOSS)2.3.CO;2
- 1130 Lin, A., Maruyama, T., Aaron, S., Michibayashi, K., Camacho, A., & Kano, K.-i.  
 1131 (2005). Propagation of seismic slip from brittle to ductile crust: Evidence from  
 1132 pseudotachylyte of the Woodroffe thrust, central Australia. *Tectonophysics*,  
 1133 402(1-4), 21–35. Retrieved from [https://www.sciencedirect.com/science/](https://www.sciencedirect.com/science/article/pii/S004019510500137X)  
 1134 [article/pii/S004019510500137X](https://www.sciencedirect.com/science/article/pii/S004019510500137X) doi: 10.1016/J.TECTO.2004.10.016
- 1135 Lindsey, E. O., & Fialko, Y. (2016). Geodetic constraints on frictional properties  
 1136 and earthquake hazard in the Imperial Valley, southern California. *Journal of*  
 1137 *Geophysical Research B: Solid Earth*, 121(2), 1097–1113. Retrieved from [http://](http://onlinelibrary.wiley.com/store/10.1002/2015JB012516/asset/jgrb51460.pdf?v=1{\\&}t=j2a5b4b4{\\&}s=5e1cb5d2e4cb866bbd855fd197d4048601908700)  
 1138 [onlinelibrary.wiley.com/store/10.1002/2015JB012516/asset/jgrb51460](http://onlinelibrary.wiley.com/store/10.1002/2015JB012516/asset/jgrb51460.pdf?v=1{\\&}t=j2a5b4b4{\\&}s=5e1cb5d2e4cb866bbd855fd197d4048601908700)  
 1139 [.pdf?v=1{\\&}t=j2a5b4b4{\\&}s=5e1cb5d2e4cb866bbd855fd197d4048601908700](http://onlinelibrary.wiley.com/store/10.1002/2015JB012516/asset/jgrb51460.pdf?v=1{\\&}t=j2a5b4b4{\\&}s=5e1cb5d2e4cb866bbd855fd197d4048601908700)  
 1140 doi: 10.1002/2015JB012516
- 1141 Liu, Y., McGuire, J. J., & Behn, M. D. (2012). Frictional behavior of oceanic trans-  
 1142 form faults and its influence on earthquake characteristics. *Journal of Geophysical*  
 1143 *Research: Solid Earth*, 117(4). Retrieved from [http://doi.wiley.com/10.1029/](http://doi.wiley.com/10.1029/2011JB009025)  
 1144 [2011JB009025](http://doi.wiley.com/10.1029/2011JB009025) doi: 10.1029/2011JB009025
- 1145 Lyzenga, G. A., Raefsky, A., & Mulligan, S. G. (1991). Models of recur-  
 1146 rent strike-slip earthquake cycles and the state of crustal stress. *Journal of*  
 1147 *Geophysical Research: Solid Earth*, 96(B13), 21623–21640. Retrieved from  
 1148 <http://doi.wiley.com/10.1029/91JB02260> doi: 10.1029/91JB02260
- 1149 Maggi, A., Jackson, J. A., McKenzie, D., & Priestley, K. (2000). Earthquake focal  
 1150 depths, effective elastic thickness, and the strength of the continental lithosphere.  
 1151 *Geology*, 28(6), 495–498. Retrieved from [http://geology.gsapubs.org/cgi/](http://geology.gsapubs.org/cgi/doi/10.1130/0091-7613(2000)28{\\%}3C495:EFDEET{\\%}3E2.0.CO;2)  
 1152 [doi/10.1130/0091-7613\(2000\)28{\\%}3C495:EFDEET{\\%}3E2.0.CO;2](http://geology.gsapubs.org/cgi/doi/10.1130/0091-7613(2000)28{\\%}3C495:EFDEET{\\%}3E2.0.CO;2) doi:  
 1153 10.1130/0091-7613(2000)28(495:EFDEET)2.0.CO;2
- 1154 Marone, C. (1998). Laboratory-derived friction laws and their application  
 1155 to seismic faulting. *Annual Review of Earth and Planetary Sciences*, 26(1),  
 1156 643–696. Retrieved from [http://www.annualreviews.org/doi/10.1146/](http://www.annualreviews.org/doi/10.1146/annurev.earth.26.1.643)  
 1157 [annurev.earth.26.1.643](http://www.annualreviews.org/doi/10.1146/annurev.earth.26.1.643) doi: 10.1146/annurev.earth.26.1.643
- 1158 Marone, C., & Kilgore, B. (1993). Scaling of the critical slip distance for seismic  
 1159 faulting with shear strain in fault zones. *Nature*, 362(6421), 618–621. Re-  
 1160 trieved from <http://www.nature.com/doi/10.1038/362618a0> doi:  
 1161 10.1038/362618a0
- 1162 Melosh, B. L., Rowe, C. D., Gerbi, C., Smit, L., & Macey, P. (2018). Seismic cy-  
 1163 cle feedbacks in a mid-crustal shear zone. *Journal of Structural Geology*, 112, 95–  
 1164 111.
- 1165 Miller, M. S., Zhang, P., & Dolan, J. F. (2014). Moho structure across the San Jac-  
 1166 into fault zone: Insights into strain localization at depth. *Lithosphere*, 6(1), 43–  
 1167 47. Retrieved from [http://lithosphere.gsapubs.org/cgi/doi/10.1130/L295.](http://lithosphere.gsapubs.org/cgi/doi/10.1130/L295.1)  
 1168 [.1](http://lithosphere.gsapubs.org/cgi/doi/10.1130/L295.1) doi: 10.1130/L295.1
- 1169 Mitchell, E. K., Fialko, Y., & Brown, K. M. (2016). Velocity-weakening behavior

- 1170 of Westerly granite at temperature up to 600 C. *Journal of Geophysical Re-*  
 1171 *search: Solid Earth*, 121(9), 6932–6946. Retrieved from [http://doi.wiley.com/](http://doi.wiley.com/10.1002/2016JB013081)  
 1172 [10.1002/2016JB013081](http://doi.wiley.com/10.1002/2016JB013081) doi: 10.1002/2016JB013081
- 1173 Miyake, Y., & Noda, H. (2019). Fully dynamic earthquake sequence simulation  
 1174 of a fault in a viscoelastic medium using a spectral boundary integral equation  
 1175 method: does interseismic stress relaxation promote aseismic transients? *Earth,*  
 1176 *Planets and Space*, 71(1), 1–12.
- 1177 Molnar, P. (1999). Continuous deformation versus faulting through the continental  
 1178 lithosphere of New Zealand. *Science*, 286(5439), 516–519. Retrieved from [http://](http://www.sciencemag.org/cgi/doi/10.1126/science.286.5439.516)  
 1179 [www.sciencemag.org/cgi/doi/10.1126/science.286.5439.516](http://www.sciencemag.org/cgi/doi/10.1126/science.286.5439.516) doi: 10.1126/  
 1180 science.286.5439.516
- 1181 Montési, L. G. (2013). Fabric development as the key for forming ductile shear  
 1182 zones and enabling plate tectonics. *Journal of Structural Geology*, 50, 254–  
 1183 266. Retrieved from [http://linkinghub.elsevier.com/retrieve/pii/](http://linkinghub.elsevier.com/retrieve/pii/S0191814113000102)  
 1184 [S0191814113000102](http://linkinghub.elsevier.com/retrieve/pii/S0191814113000102) doi: 10.1016/j.jsg.2012.12.011
- 1185 Montési, L. G., & Zuber, M. T. (2002). A unified description of localization  
 1186 for application to large-scale tectonics. *Journal of Geophysical Research*,  
 1187 107(B3). Retrieved from <http://doi.wiley.com/10.1029/2001JB000465> doi:  
 1188 10.1029/2001JB000465
- 1189 Moore, J. D., & Parsons, B. (2015). Scaling of viscous shear zones with  
 1190 depth-dependent viscosity and power-law stress-strain-rate dependence. *Geo-*  
 1191 *physical Journal International*, 202(1), 242–260. Retrieved from [http://](http://academic.oup.com/gji/article/202/1/242/589272/Scaling-of-viscous-shear-zones-with-depthdependent)  
 1192 [academic.oup.com/gji/article/202/1/242/589272/Scaling-of-viscous](http://academic.oup.com/gji/article/202/1/242/589272/Scaling-of-viscous-shear-zones-with-depthdependent)  
 1193 [-shear-zones-with-depthdependent](http://academic.oup.com/gji/article/202/1/242/589272/Scaling-of-viscous-shear-zones-with-depthdependent) doi: 10.1093/gji/ggv143
- 1194 Neumann, F., Negrete-Aranda, R., Harris, R. N., Contreras, J., Sclater, J. G., &  
 1195 González-Fernández, A. (2017). Systematic heat flow measurements across the  
 1196 Wagner Basin, northern Gulf of California. *Earth and Planetary Science Letters*,  
 1197 479, 340–353. Retrieved from <https://doi.org/10.1016/j.epsl.2017.09.037>  
 1198 doi: 10.1016/j.epsl.2017.09.037
- 1199 Noda, H., Dunham, E. M., & Rice, J. R. (2009). Earthquake ruptures with thermal  
 1200 weakening and the operation of major faults at low overall stress levels. *Journal*  
 1201 *of Geophysical Research*, 114. Retrieved from [http://doi.wiley.com/10.1029/](http://doi.wiley.com/10.1029/2008JB006143)  
 1202 [2008JB006143](http://doi.wiley.com/10.1029/2008JB006143) doi: 10.1029/2008JB006143
- 1203 Noda, H., & Lapusta, N. (2010). Three-dimensional earthquake sequence simula-  
 1204 tions with evolving temperature and pore pressure due to shear heating: Effect of  
 1205 heterogeneous hydraulic diffusivity. *Journal of Geophysical Research: Solid Earth*,  
 1206 115(B12314). Retrieved from <http://doi.wiley.com/10.1029/2010JB007780>  
 1207 doi: 10.1029/2010JB007780
- 1208 Noda, H., & Shimamoto, T. (2005). Thermal pressurization and slip-weakening  
 1209 distance of a fault: An example of the Hanaore fault, southwest Japan. *Bul-*  
 1210 *letin of the Seismological Society of America*, 95(4), 1224–1233. Retrieved from  
 1211 <https://pubs.geoscienceworld.org/bssa/article/95/4/1224-1233/121052>  
 1212 doi: 10.1785/0120040089
- 1213 Norris, R. J., & Cooper, A. F. (2003). Very high strains recorded in mylonites  
 1214 along the Alpine Fault, New Zealand: Implications for the deep structure of  
 1215 plate boundary faults. *Journal of Structural Geology*, 25(12), 2141–2157.  
 1216 Retrieved from [http://www.sciencedirect.com/science/article/pii/](http://www.sciencedirect.com/science/article/pii/S0191814103000452)  
 1217 [S0191814103000452](http://www.sciencedirect.com/science/article/pii/S0191814103000452) doi: 10.1016/S0191-8141(03)00045-2
- 1218 Norris, R. J., & Toy, V. G. (2014). *Continental transforms: A view from the Alpine*  
 1219 *Fault* (Vol. 64). Pergamon. Retrieved from [http://www.sciencedirect.com/](http://www.sciencedirect.com/science/article/pii/S0191814114000601)  
 1220 [science/article/pii/S0191814114000601](http://www.sciencedirect.com/science/article/pii/S0191814114000601) doi: 10.1016/j.jsg.2014.03.003
- 1221 Petley-Ragan, A., Ben-Zion, Y., Austrheim, H., Ildefonse, B., Renard, F., &  
 1222 Jamtveit, B. (2019). Dynamic earthquake rupture in the lower crust. *Science*  
 1223 *advances*, 5(7), eaaw0913.

- 1224 Platt, J. P., & Behr, W. M. (2011). Deep structure of lithospheric fault zones.  
 1225 *Geophysical Research Letters*, *38*(24). Retrieved from [http://doi.wiley.com/](http://doi.wiley.com/10.1029/2011GL049719)  
 1226 [10.1029/2011GL049719](http://doi.wiley.com/10.1029/2011GL049719) doi: 10.1029/2011GL049719
- 1227 Rempel, A. W., & Rice, J. R. (2006). Thermal pressurization and onset of melting  
 1228 in fault zones. *Journal of Geophysical Research: Solid Earth*, *111*(B9).
- 1229 Rice, J. R. (1992). Chapter 20 Fault Stress States, pore pressure distributions,  
 1230 and the weakness of the San Andreas Fault. *International Geophysics*, *51*(C),  
 1231 475–503. Retrieved from [http://linkinghub.elsevier.com/retrieve/pii/](http://linkinghub.elsevier.com/retrieve/pii/S0074614208628351)  
 1232 [S0074614208628351](http://linkinghub.elsevier.com/retrieve/pii/S0074614208628351) doi: 10.1016/S0074-6142(08)62835-1
- 1233 Rice, J. R. (1993). Spatiotemporal complexity of slip on a fault. *Journal of Geo-*  
 1234 *physical Research*, *98*(B6), 9885–9907. Retrieved from [http://doi.wiley.com/10](http://doi.wiley.com/10.1029/93JB00191)  
 1235 [.1029/93JB00191](http://doi.wiley.com/10.1029/93JB00191) doi: 10.1029/93JB00191
- 1236 Rice, J. R. (2006). Heating and weakening of faults during earthquake slip. *Journal*  
 1237 *of Geophysical Research: Solid Earth*, *111*(5). Retrieved from [http://doi.wiley](http://doi.wiley.com/10.1029/2005JB004006)  
 1238 [.com/10.1029/2005JB004006](http://doi.wiley.com/10.1029/2005JB004006) doi: 10.1029/2005JB004006
- 1239 Rice, J. R., Lapusta, N., & Ranjith, K. (2001). Rate and state dependent fric-  
 1240 tion and the stability of sliding between elastically deformable solids. *Jour-*  
 1241 *nal of the Mechanics and Physics of Solids*, *49*, 1865–1898. Retrieved from  
 1242 <http://linkinghub.elsevier.com/retrieve/pii/S0022509601000424> doi:  
 1243 [10.1016/S0022-5096\(01\)00042-4](http://linkinghub.elsevier.com/retrieve/pii/S0022509601000424)
- 1244 Rosenberg, C. L., & Schneider, S. (2008). The western termination of the SEMP  
 1245 Fault (eastern Alps) and its bearing on the exhumation of the Tauern Window.  
 1246 *Geological Society Special Publication*, *298*, 197–218. doi: 10.1144/SP298.10
- 1247 Ruina, A. (1983). Slip instability and state variable friction laws. *Journal of Geo-*  
 1248 *physical Research: Solid Earth*, *88*(B12), 10359–10370. Retrieved from [http://](http://doi.wiley.com/10.1029/JB088iB12p10359)  
 1249 [doi.wiley.com/10.1029/JB088iB12p10359](http://doi.wiley.com/10.1029/JB088iB12p10359) doi: 10.1029/JB088iB12p10359
- 1250 Rybacki, E., & Dresen, G. (2004). Deformation mechanism maps for feldspar  
 1251 rocks. *Tectonophysics*, *382*(3-4), 173–187. Retrieved from [https://ac.els](https://ac.els-cdn.com/S0040195104000186/1-s2.0-S0040195104000186-main.pdf?{\_}tid=be6857c2-fb16-11e7-b706-00000aacb361{\&}acdnat=1516146264{\_}jdda4e347dad556b799c0dbf083f6075c)  
 1252 [-cdn.com/S0040195104000186/1-s2.0-S0040195104000186-main.pdf?{\](https://ac.els-cdn.com/S0040195104000186/1-s2.0-S0040195104000186-main.pdf?{\_}tid=be6857c2-fb16-11e7-b706-00000aacb361{\&}acdnat=1516146264{\_}jdda4e347dad556b799c0dbf083f6075c)  
 1253 [\\_}tid=be6857c2-fb16-11e7-b706-00000aacb361{\&}acdnat=1516146264{\](https://ac.els-cdn.com/S0040195104000186/1-s2.0-S0040195104000186-main.pdf?{\_}tid=be6857c2-fb16-11e7-b706-00000aacb361{\&}acdnat=1516146264{\_}jdda4e347dad556b799c0dbf083f6075c)  
 1254 [\\_}jdda4e347dad556b799c0dbf083f6075c](https://ac.els-cdn.com/S0040195104000186/1-s2.0-S0040195104000186-main.pdf?{\_}tid=be6857c2-fb16-11e7-b706-00000aacb361{\&}acdnat=1516146264{\_}jdda4e347dad556b799c0dbf083f6075c) doi: 10.1016/j.tecto.2004.01.006
- 1255 Rybacki, E., Gottschalk, M., Wirth, R., & Dresen, G. (2006). Influence of wa-  
 1256 ter fugacity and activation volume on the flow properties of fine-grained anor-  
 1257 thite aggregates. *Journal of Geophysical Research: Solid Earth*, *111*(B3), n/a–  
 1258 n/a. Retrieved from <http://doi.wiley.com/10.1029/2005JB003663> doi:  
 1259 [10.1029/2005JB003663](http://doi.wiley.com/10.1029/2005JB003663)
- 1260 Sass, J. H., Williams, C. F., Lachenbruch, A. H., Galanis, S. P. J., & Grubb, F. V.  
 1261 (1997). Thermal regime of the San Andreas fault near Parkfield, California. *Jour-*  
 1262 *nal of Geophysical Research*, *102*, 27,527–575,586.
- 1263 Savage, J. C., & Lachenbruch, A. H. (2003). Consequences of viscous drag  
 1264 beneath a transform fault. *Journal of Geophysical Research: Solid Earth*,  
 1265 *108*(B1). Retrieved from <http://doi.wiley.com/10.1029/2001JB000711> doi:  
 1266 [10.1029/2001JB000711](http://doi.wiley.com/10.1029/2001JB000711)
- 1267 Savage, J. C., & Prescott, W. H. (1978). Asthenosphere readjustment and the earth-  
 1268 quake cycle. *Journal of Geophysical Research*, *83*(B7), 3369–3376. Retrieved from  
 1269 <http://onlinelibrary.wiley.com/doi/10.1029/JB083iB07p03369/full> doi:  
 1270 [10.1029/JB083iB07p03369](http://onlinelibrary.wiley.com/doi/10.1029/JB083iB07p03369/full)
- 1271 Searle, M. P., Yeh, M. W., Lin, T. H., & Chung, S. L. (2010). Structural constraints  
 1272 on the timing of left-lateral shear along the red river shear zone in the ailao shan  
 1273 and diancang shan ranges, Yunnan, SW China. *Geosphere*, *6*(4), 316–338. doi:  
 1274 [10.1130/GES00580.1](http://doi.wiley.com/10.1130/GES00580.1)
- 1275 Shelly, D. R. (2010). Migrating tremors illuminate complex deformation be-  
 1276 neath the seismogenic San Andreas fault. *Nature*, *463*(7281), 648–652. Re-  
 1277 [trieved from <https://www.nature.com/nature/journal/v463/n7281/pdf/>](https://www.nature.com/nature/journal/v463/n7281/pdf/)

- 1278 nature08755.pdf<http://www.ncbi.nlm.nih.gov/pubmed/20130648> doi:  
1279 10.1038/nature08755
- 1280 Shimamoto, T., & Noda, H. (2014). A friction to flow constitutive law and its appli-  
1281 cation to a 2-D modeling of earthquakes. *Journal of Geophysical Research: Solid*  
1282 *Earth*, 119(11), 8089–8106. Retrieved from [http://doi.wiley.com/10.1002/](http://doi.wiley.com/10.1002/2014JB011170)  
1283 2014JB011170 doi: 10.1002/2014JB011170
- 1284 Sibson, R. H. (1974). Frictional constraints on thrust, wrench and normal faults.  
1285 *Nature*, 249, 542–544. Retrieved from [http://www.nature.com/doifinder/](http://www.nature.com/doifinder/10.1038/249542a0)  
1286 10.1038/249542a0 doi: 10.1038/249542a0
- 1287 Sibson, R. H. (1982). Fault zone models, heat flow, and the depth distribution of  
1288 earthquakes in the continental crust of the United States. *Bulletin of the Seismo-*  
1289 *logical Society of America*, 72(1), 151–163.
- 1290 Sibson, R. H. (1984). Roughness at the base of the seismogenic zone: Contributing  
1291 factors. *Journal of Geophysical Research*, 89. doi: 10.1029/JB089iB07p05791
- 1292 Sibson, R. H. (2003). Thickness of the seismic slip zone. *Bulletin of the Seis-*  
1293 *mological Society of America*, 93(3), 1169–1178. Retrieved from [https://](https://gsw.silverchair-cdn.com/gsw/Content{\_}public/Journal/bssa/93/3/10.1785{\_}0120020061/4/1169.pdf?Expires=2147483647{\&}Signature=Uzay8NnoHacPNXjjEaNsm5ZwsgOE3F{\~}MWUdq2Es2wcb0jYCzWd4rDRkN25iOK{\~}1p05PjU{\~}aAmWJDFQnLyPsdMhGgZG{\~}-U3ax4S{\~}k{\~}zMxcJwv)  
1294 [gsw.silverchair-cdn.com/gsw/Content{\\\_}public/Journal/bssa/93/3/](https://gsw.silverchair-cdn.com/gsw/Content{\_}public/Journal/bssa/93/3/10.1785{\_}0120020061/4/1169.pdf?Expires=2147483647{\&}Signature=Uzay8NnoHacPNXjjEaNsm5ZwsgOE3F{\~}MWUdq2Es2wcb0jYCzWd4rDRkN25iOK{\~}1p05PjU{\~}aAmWJDFQnLyPsdMhGgZG{\~}-U3ax4S{\~}k{\~}zMxcJwv)  
1295 [10.1785{\\\_}0120020061/4/1169.pdf?Expires=2147483647{\&}Signature=](https://gsw.silverchair-cdn.com/gsw/Content{\_}public/Journal/bssa/93/3/10.1785{\_}0120020061/4/1169.pdf?Expires=2147483647{\&}Signature=Uzay8NnoHacPNXjjEaNsm5ZwsgOE3F{\~}MWUdq2Es2wcb0jYCzWd4rDRkN25iOK{\~}1p05PjU{\~}aAmWJDFQnLyPsdMhGgZG{\~}-U3ax4S{\~}k{\~}zMxcJwv)  
1296 [Uzay8NnoHacPNXjjEaNsm5ZwsgOE3F{\~}MWUdq2Es2wcb0jYCzWd4rDRkN25iOK{\~}1p05PjU{\~}aAmWJDFQnLyPsdMhGgZG{\~}](https://gsw.silverchair-cdn.com/gsw/Content{\_}public/Journal/bssa/93/3/10.1785{\_}0120020061/4/1169.pdf?Expires=2147483647{\&}Signature=Uzay8NnoHacPNXjjEaNsm5ZwsgOE3F{\~}MWUdq2Es2wcb0jYCzWd4rDRkN25iOK{\~}1p05PjU{\~}aAmWJDFQnLyPsdMhGgZG{\~}-U3ax4S{\~}k{\~}zMxcJwv)  
1297 [-U3ax4S{\~}k{\~}zMxcJwv](https://gsw.silverchair-cdn.com/gsw/Content{\_}public/Journal/bssa/93/3/10.1785{\_}0120020061/4/1169.pdf?Expires=2147483647{\&}Signature=Uzay8NnoHacPNXjjEaNsm5ZwsgOE3F{\~}MWUdq2Es2wcb0jYCzWd4rDRkN25iOK{\~}1p05PjU{\~}aAmWJDFQnLyPsdMhGgZG{\~}-U3ax4S{\~}k{\~}zMxcJwv) doi: 10.1785/0120020061
- 1298 Sibson, R. H., & Toy, V. G. (2006). The habitat of fault-generated pseudotachy-  
1299 lyte: Presence vs. absence of friction-melt. *Earthquakes: Radiated Energy and the*  
1300 *Physics of Faulting*, 153–166. Retrieved from [http://www.agu.org/books/gm/](http://www.agu.org/books/gm/v170/170GM16/170GM16.shtml)  
1301 v170/170GM16/170GM16.shtml doi: 10.1029/170GM16
- 1302 Takeuchi, C. S., & Fialko, Y. (2012). Dynamic models of interseismic deformation  
1303 and stress transfer from plate motion to continental transform faults. *Journal*  
1304 *of Geophysical Research*, 117(B5), n/a–n/a. Retrieved from [http://doi.wiley](http://doi.wiley.com/10.1029/2011JB009056)  
1305 [.com/10.1029/2011JB009056](http://doi.wiley.com/10.1029/2011JB009056) doi: 10.1029/2011JB009056
- 1306 Takeuchi, C. S., & Fialko, Y. (2013). On the effects of thermally weakened ductile  
1307 shear zones on postseismic deformation. *Journal of Geophysical Research: Solid*  
1308 *Earth*, 118(12), 6295–6310. Retrieved from [http://doi.wiley.com/10.1002/](http://doi.wiley.com/10.1002/2013JB010215)  
1309 2013JB010215 doi: 10.1002/2013JB010215
- 1310 Tembe, S., Lockner, D., & Wong, T. F. (2009). Constraints on the stress  
1311 state of the San Andreas Fault with analysis based on core and cuttings from  
1312 San Andreas Fault Observatory at Depth (SAFOD) drilling phases 1 and  
1313 2. *Journal of Geophysical Research: Solid Earth*, 114(11). Retrieved from  
1314 <http://doi.wiley.com/10.1029/2008JB005883> doi: 10.1029/2008JB005883
- 1315 Thatcher, W. (1983). Nonlinear strain buildup and the earthquake cycle on the  
1316 San Andreas Fault. *Journal of Geophysical Research*, 88(B7), 5893–5902. doi: 10  
1317 .1029/JB088iB07p05893
- 1318 Thatcher, W., & Chapman, D. (2018). Heat Flow Data and Seismic Imaging Reveal  
1319 Both Transient and Steady-State Thermo-Mechanical Processes at Work Beneath  
1320 Southern California. *AGU Fall Meeting Abstracts, 2018*, T52D–08.
- 1321 Thatcher, W., & England, P. C. (1998). Ductile shear zones beneath strike-slip  
1322 faults: Implications for the thermomechanics or the San Andreas fault zone. *Jour-*  
1323 *nal of Geophysical Research*, 103(B1), 891–905.
- 1324 Thatcher, W., & Pollitz, F. F. (2008). Temporal evolution of continental lithospheric  
1325 strength in actively deforming regions. *GSA Today*, 18(4/5), 4–11. Retrieved from  
1326 [ftp://portcullis.earth.ox.ac.uk/pub/tony/mike/Thatcher{\\\_}Pollitz{\\\_}](ftp://portcullis.earth.ox.ac.uk/pub/tony/mike/Thatcher{\_}Pollitz{\_}2007{\_}submitted.pdf)  
1327 [\\_}2007{\\\_}submitted.pdf](ftp://portcullis.earth.ox.ac.uk/pub/tony/mike/Thatcher{\_}Pollitz{\_}2007{\_}submitted.pdf) doi: 10.1130/GSATO1804-5A.1
- 1328 Tse, S. T., & Rice, J. R. (1986). Crustal earthquake instability in relation to the  
1329 depth variation of frictional slip properties. *Journal of Geophysical Research*,  
1330 91(B9), 9452–9472. doi: 10.1029/JB091iB09p09452
- 1331 Tullis, T. E., & Weeks, J. D. (1986). Constitutive behavior and stability of fric-

- 1332 tional sliding of granite. *Pure and Applied Geophysics PAGEOPH*. doi: 10.1007/  
1333 BF00877209
- 1334 Turcotte, D. L., & Schubert, G. (2002). *Geodynamics* (2nd ed.). Cambridge Univer-  
1335 sity Press.
- 1336 Vauchez, A., & Tommasi, A. (2003). Wrench faults down to the asthenosphere:  
1337 geological and geophysical evidence and thermomechanical effects. *Geological*  
1338 *Society, London, Special Publications*, 210(1), 15–34. Retrieved from [http://](http://sp.lyellcollection.org/lookup/doi/10.1144/GSL.SP.2003.210.01.02)  
1339 [sp.lyellcollection.org/lookup/doi/10.1144/GSL.SP.2003.210.01.02](http://sp.lyellcollection.org/lookup/doi/10.1144/GSL.SP.2003.210.01.02) doi:  
1340 10.1144/GSL.SP.2003.210.01.02
- 1341 Visser, R. L. M., Drury, M. R., Newman, J., & Fliervoet, T. E. (1997). Mylonitic  
1342 deformation in upper mantle peridotites of the North Pyrenean Zone (France):  
1343 implications for strength and strain localization in the lithosphere. *Tectono-*  
1344 *physics*, 279, 303–325.
- 1345 Warren, J. M., & Hirth, G. (2006). Grain size sensitive deformation mechanisms in  
1346 naturally deformed peridotites. *Earth and Planetary Science Letters*, 248(1-2),  
1347 423–435. Retrieved from [http://www.sciencedirect.com/science/article/](http://www.sciencedirect.com/science/article/pii/S0012821X06004225)  
1348 [pii/S0012821X06004225](http://www.sciencedirect.com/science/article/pii/S0012821X06004225) doi: 10.1016/j.epsl.2006.06.006
- 1349 Weber, M., Abu-Ayyash, K., Abueladas, A., Agnon, A., Al-Amoush, H.,  
1350 Babeyko, A., ... Wylegalla, K. (2004). The crustal structure of the  
1351 Dead Sea Transform. *Geophysical Journal International*, 156, 655–681.  
1352 Retrieved from [https://oup.silverchair-cdn.com/oup/backfile/](https://oup.silverchair-cdn.com/oup/backfile/Content{\_}public/Journal/gji/156/3/10.1111/j.1365-246X.2004.02143.x/2/156-3-655.pdf?Expires=1494900268{\&}Signature=08gIFFx9boL7I9SHyBKLq{\~}vUyDryZjC2dXdFYNgqEsPKERd8Zm0HrULPJtVEMlxxxvX4LTgM9Hy-DTE1B9mOXEvUb0EBRRuyYvV)  
1353 [Content{\\\_}public/Journal/gji/156/3/10.1111/j.1365-246X.2004](https://oup.silverchair-cdn.com/oup/backfile/Content{\_}public/Journal/gji/156/3/10.1111/j.1365-246X.2004.02143.x/2/156-3-655.pdf?Expires=1494900268{\&}Signature=08gIFFx9boL7I9SHyBKLq{\~}vUyDryZjC2dXdFYNgqEsPKERd8Zm0HrULPJtVEMlxxxvX4LTgM9Hy-DTE1B9mOXEvUb0EBRRuyYvV)  
1354 [.02143.x/2/156-3-655.pdf?Expires=1494900268{\&}Signature=](https://oup.silverchair-cdn.com/oup/backfile/Content{\_}public/Journal/gji/156/3/10.1111/j.1365-246X.2004.02143.x/2/156-3-655.pdf?Expires=1494900268{\&}Signature=08gIFFx9boL7I9SHyBKLq{\~}vUyDryZjC2dXdFYNgqEsPKERd8Zm0HrULPJtVEMlxxxvX4LTgM9Hy-DTE1B9mOXEvUb0EBRRuyYvV)  
1355 [08gIFFx9boL7I9SHyBKLq{\~}vUyDryZjC2dXdFYNgqEsPKERd8Zm0HrULPJtVEMlxxxvX4LTgM9Hy](https://oup.silverchair-cdn.com/oup/backfile/Content{\_}public/Journal/gji/156/3/10.1111/j.1365-246X.2004.02143.x/2/156-3-655.pdf?Expires=1494900268{\&}Signature=08gIFFx9boL7I9SHyBKLq{\~}vUyDryZjC2dXdFYNgqEsPKERd8Zm0HrULPJtVEMlxxxvX4LTgM9Hy-DTE1B9mOXEvUb0EBRRuyYvV)  
1356 [-DTE1B9mOXEvUb0EBRRuyYvV](https://oup.silverchair-cdn.com/oup/backfile/Content{\_}public/Journal/gji/156/3/10.1111/j.1365-246X.2004.02143.x/2/156-3-655.pdf?Expires=1494900268{\&}Signature=08gIFFx9boL7I9SHyBKLq{\~}vUyDryZjC2dXdFYNgqEsPKERd8Zm0HrULPJtVEMlxxxvX4LTgM9Hy-DTE1B9mOXEvUb0EBRRuyYvV) doi: 10.1111/j.1365-246X.2004.02143.x
- 1357 Weijermars, R. (1987). The Palomares brittle-ductile Shear Zone of  
1358 southern Spain. *Journal of Structural Geology*, 9(2), 130–157. Re-  
1359 trieved from [https://ac-els-cdn-com.stanford.idm.oclc.org/](https://ac-els-cdn-com.stanford.idm.oclc.org/0191814187900228/1-s2.0-0191814187900228-main.pdf?{\_}tid=2c3d520d-d817-4e00-9c30-f5b15d8aead8{\&}acdnat=1533233889{\_}82fddfc8895a6699400bfe3ea8e2587)  
1360 [0191814187900228/1-s2.0-0191814187900228-main.pdf?{\\\_}tid=](https://ac-els-cdn-com.stanford.idm.oclc.org/0191814187900228/1-s2.0-0191814187900228-main.pdf?{\_}tid=2c3d520d-d817-4e00-9c30-f5b15d8aead8{\&}acdnat=1533233889{\_}82fddfc8895a6699400bfe3ea8e2587)  
1361 [2c3d520d-d817-4e00-9c30-f5b15d8aead8{\&}acdnat=1533233889{\](https://ac-els-cdn-com.stanford.idm.oclc.org/0191814187900228/1-s2.0-0191814187900228-main.pdf?{\_}tid=2c3d520d-d817-4e00-9c30-f5b15d8aead8{\&}acdnat=1533233889{\_}82fddfc8895a6699400bfe3ea8e2587)  
1362 [\\_}82fddfc8895a6699400bfe3ea8e2587](https://ac-els-cdn-com.stanford.idm.oclc.org/0191814187900228/1-s2.0-0191814187900228-main.pdf?{\_}tid=2c3d520d-d817-4e00-9c30-f5b15d8aead8{\&}acdnat=1533233889{\_}82fddfc8895a6699400bfe3ea8e2587)
- 1363 White, J. C. (2012). Paradoxical pseudotachylyte - Fault melt outside the seismo-  
1364 genic zone. *Journal of Structural Geology*, 38, 11–20. Retrieved from [http://dx](http://dx.doi.org/10.1016/j.jsg.2011.11.016)  
1365 [.doi.org/10.1016/j.jsg.2011.11.016](http://dx.doi.org/10.1016/j.jsg.2011.11.016) doi: 10.1016/j.jsg.2011.11.016
- 1366 Wibberley, C. A., & Shimamoto, T. (2002). Internal structure and permeability  
1367 of major strike-slip fault zones: The Median Tectonic Line in Mie Prefecture,  
1368 Southwest Japan. *Journal of Structural Geology*, 25(1), 59–78. Retrieved from  
1369 [www.elsevier.com/locate/jsg](http://www.elsevier.com/locate/jsg) doi: 10.1016/S0191-8141(02)00014-7
- 1370 Williams, C. F., & DeAngelo, J. (2011). Evaluation of approaches and uncertain-  
1371 ties in estimation of temperature in the upper crust of the western United States.  
1372 *GRC Transactions*, 35, 1599 – 1606.
- 1373 Wilson, C. K., Jones, C. H., Molnar, P., Sheehan, A. F., & Boyd, O. S. (2004). Dis-  
1374 tributed deformation in the lower crust and upper mantle beneath a continental  
1375 strike-slip fault zone: Marlborough Fault System, South Island, New Zealand.  
1376 *Geology*, 32(10), 837–840. Retrieved from [http://geology.gsapubs.org/](http://geology.gsapubs.org/cgi/doi/10.1130/G20657.1)  
1377 [cgi/doi/10.1130/G20657.1](http://geology.gsapubs.org/cgi/doi/10.1130/G20657.1)[http://geology.gsapubs.org/content/32/10/](http://geology.gsapubs.org/content/32/10/837.short)  
1378 [837.short](http://geology.gsapubs.org/content/32/10/837.full.pdf)[.full.pdf](http://geology.gsapubs.org/content/32/10/837.full.pdf) doi:  
1379 10.1130/G20657.1
- 1380 Wright, T. J., Elliott, J. R., Wang, H., & Ryder, I. (2013). Earthquake cycle de-  
1381 formation and the Moho: Implications for the rheology of continental lithosphere.  
1382 *Tectonophysics*, 609, 504–523. Retrieved from [http://dx.doi.org/10.1016/](http://dx.doi.org/10.1016/j.tecto.2013.07.029)  
1383 [j.tecto.2013.07.029](http://dx.doi.org/10.1016/j.tecto.2013.07.029)[http://www.sciencedirect.com/science/article/pii/](http://www.sciencedirect.com/science/article/pii/S0040195113004708)  
1384 [S0040195113004708](http://www.sciencedirect.com/science/article/pii/S0040195113004708) doi: 10.1016/j.tecto.2013.07.029
- 1385 Yang, Y., & Forsyth, D. W. (2008). Attenuation in the upper mantle be-

1386 neath southern California: Physical state of the lithosphere and astheno-  
1387 sphere. *Journal of Geophysical Research: Solid Earth*, 113(3). Retrieved from  
1388 <http://doi.wiley.com/10.1029/2007JB005118> doi: 10.1029/2007JB005118  
1389 Zhang, X., & Sagiya, T. (2017). Shear strain concentration mechanism in  
1390 the lower crust below an intraplate strike-slip fault based on rheological  
1391 laws of rocks. *Earth, Planets and Space*, 69(1). Retrieved from [https://](https://link.springer.com/content/pdf/10.1186/s40623-017-0668-5.pdf)  
1392 [link.springer.com/content/pdf/10.1186/s40623-017-0668-5.pdf](https://link.springer.com/content/pdf/10.1186/s40623-017-0668-5.pdf)  
1393 doi: 10.1186/s40623-017-0668-5  
1394 Zhu, L. (2000). Crustal structure across the San Andreas Fault, south-  
1395 ern California from teleseismic converted waves. *Earth and Planetary Sci-*  
1396 *ence Letters*, 179, 183–190. Retrieved from [http://ac.els-cdn.com/](http://ac.els-cdn.com/S0012821X00001011/1-s2.0-S0012821X00001011-main.pdf?tid=60486596-3902-11e7-a44a-00000aacb360&acdnat=1494806982-f5335d669505f121c0afc32db93f3935)  
1397 [S0012821X00001011/1-s2.0-S0012821X00001011-main.pdf?tid=](http://ac.els-cdn.com/S0012821X00001011/1-s2.0-S0012821X00001011-main.pdf?tid=60486596-3902-11e7-a44a-00000aacb360&acdnat=1494806982-f5335d669505f121c0afc32db93f3935)  
1398 [60486596-3902-11e7-a44a-00000aacb360&acdnat=1494806982-](http://ac.els-cdn.com/S0012821X00001011/1-s2.0-S0012821X00001011-main.pdf?tid=60486596-3902-11e7-a44a-00000aacb360&acdnat=1494806982-f5335d669505f121c0afc32db93f3935)  
1399 [f5335d669505f121c0afc32db93f3935](http://ac.els-cdn.com/S0012821X00001011/1-s2.0-S0012821X00001011-main.pdf?tid=60486596-3902-11e7-a44a-00000aacb360&acdnat=1494806982-f5335d669505f121c0afc32db93f3935)

# Supporting Information for “Influence of Shear Heating and Thermomechanical Coupling on Earthquake Sequences and the Brittle-Ductile Transition”

Kali L. Allison<sup>1,2</sup>, Eric M. Dunham<sup>1,3</sup>

<sup>1</sup>Department of Geophysics, Stanford University, Stanford, California, USA

<sup>2</sup>now at: Department of Geology, University of Maryland, College Park, Maryland, USA

<sup>3</sup>Institute for Computational and Mathematical Engineering, Stanford University, Stanford, California, USA

## 1. Numerical Method

The discretization of the governing equations is a straightforward extension of previous work. We employ the Cartesian grid finite difference method developed by Erickson & Dunham (2014) and Allison & Dunham (2018) to solve the static elasticity and heat equations, both on the same grid. We select the along-fault grid spacing to resolve the nucleation length (e.g., Ruina, 1983; Rice, 1983, 1993; Rice et al., 2001),

$$h^* = \frac{\mu d_c}{\sigma_n(b-a)} \quad (1)$$

and the cohesive-zone size (Dieterich, 1992; Ampuero & Rubin, 2008),

$$L_b = \frac{\mu d_c}{\sigma_n b}, \quad (2)$$

which is generally smaller than  $h^*$ . In the fault-normal direction, we must resolve thermal boundary layers near the fault, the width of which will be no larger than  $w$ . Therefore, we use a grid spacing of  $L_b/4$  in the  $z$ -direction in the seismogenic zone, and  $w/5$  in the  $y$ -direction near the fault, with aggressive grid stretching outside of this region.

We next explain time stepping. We utilize the explicit Runge–Kutta algorithm with adaptive time-step selection described in Allison & Dunham (2018) to update slip, state variable, and viscous strains. However, stiffness of the heat equation requires implicit time-stepping for efficiency. To handle this, we use operator splitting, updating temperature in the heat equation with backward Euler after each full adaptive step.

Specifically, during each adaptive Runge–Kutta time step from time  $t^n$  to  $t^{n+1} = t^n + \Delta t$ , temperature is held fixed at  $\Delta T^n$  while solving for slip  $\delta^{n+1}$ , state  $\psi^{n+1}$ , and the viscous strains  $\gamma_{xy}^{n+1}$  and  $\gamma_{xz}^{n+1}$ . We then compute the stresses at  $t^{n+1}$ , and the flow law provides the viscous strain rates  $\dot{\gamma}_{xy}^{n+1}$  and  $\dot{\gamma}_{xz}^{n+1}$ . Then, these fields are held fixed and used to compute the shear heating source term  $Q^{n+1}$  when solving for  $\Delta T^{n+1}$ .

## 2. Stresses

The similarities and differences between these three simulations featured in Figure 4 can also be seen in the temporal evolution of shear stress on the fault and its deep extension, plotted in Figure S1. In the upper crust, the shear stress is very similar in all three simulations, because the off-fault material is effectively elastic and stress is limited by the frictional strength of the fault. At greater depths, around 23 km in the viscoelastic simulation without shear heating and 15 km in the viscoelastic simulation with shear heating, the viscoelastic material becomes much weaker than the frictional strength of the fault, resulting in a much weaker shear stress than in the elastic simulation.

## 3. Influence of Pore Pressure on Contributions to Shear Heating

Figure S2 explores the influence of pore pressure, parametrized through  $\lambda$ , on the thermal anomaly.

## 4. Thermal Energy

One way of summarizing the results of our parameter space search is to integrate the thermal anomaly times the heat capacity over the domain, producing the thermal energy per unit length  $\theta$ . As shown in Figure S3, the total thermal energy increases with deeper LAB depths. It also decreases slightly with increasing pore pressure, but this is a much smaller effect. Also, for all the parameters considered, both frictional and viscous shear heating contribute substantially to the total thermal energy in the system, with viscous shear heating constituting more than half the total (except for the simulation with a 70 km deep LAB and  $\lambda = 0.8$ ).

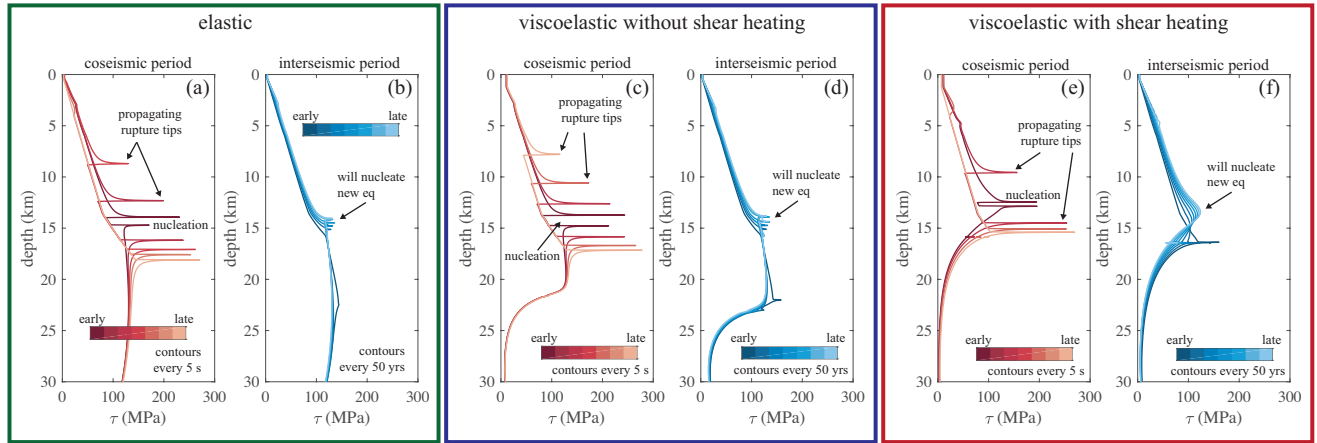


**Figure S1.** Comparison of the temporal evolution of shear stress on the fault and its deep extension in elastic, viscoelastic without shear heating, and viscoelastic with shear heating cycle simulations, for an LAB of 50 km and hydrostatic pore pressure. (a), (c) and (e) First 20 s of the coseismic period, with contours plotted every 5 s. (b), (d) and (f) Interseismic period with contours plotted every 50 years.

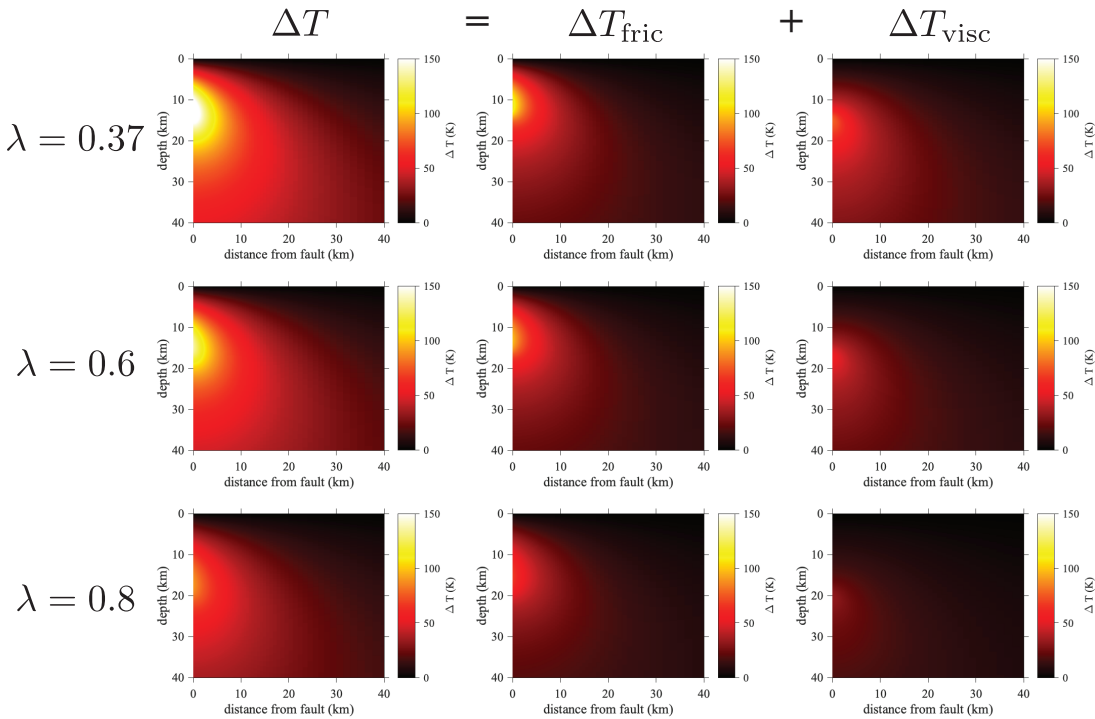


**Figure S2.** Comparison of  $\Delta T$  and its components  $\Delta T_{\text{fric}}$  and  $\Delta T_{\text{visc}}$ , as a function of  $\lambda$ , for a simulation with a 50 km deep LAB.

## 5. Temperatures of Various Transitions

40 The temperatures which correspond with the depths plotted in Figure 8 are shown in Figure S4.

## 6. Comparison of Steady-State and Cycle-Averaged Results

41 Figures S5 and S6 compare steady-state and cycle-averaged results.

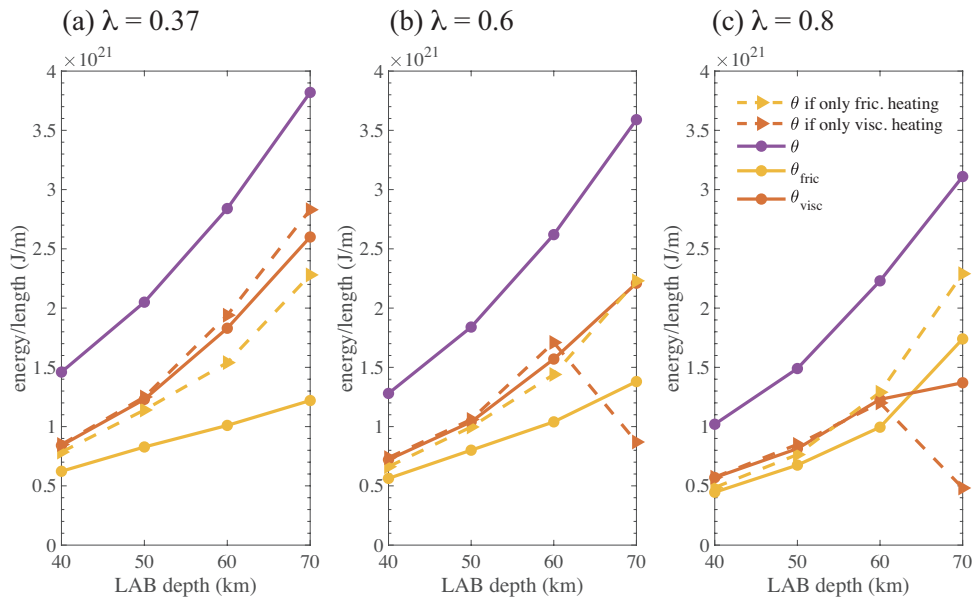


**Figure S3.** Total thermal energy  $\theta$  (purple), portion of total thermal energy contributed by frictional  $\theta_{\text{fric}}$  (yellow, solid lines) and viscous  $\theta_{\text{visc}}$  (red, solid lines) shear heating, total energy from simulations with only frictional shear heating (yellow, dashed lines), and total energy from simulations with only viscous shear heating (red, dashed lines), as a function of LAB depth and pore pressure.

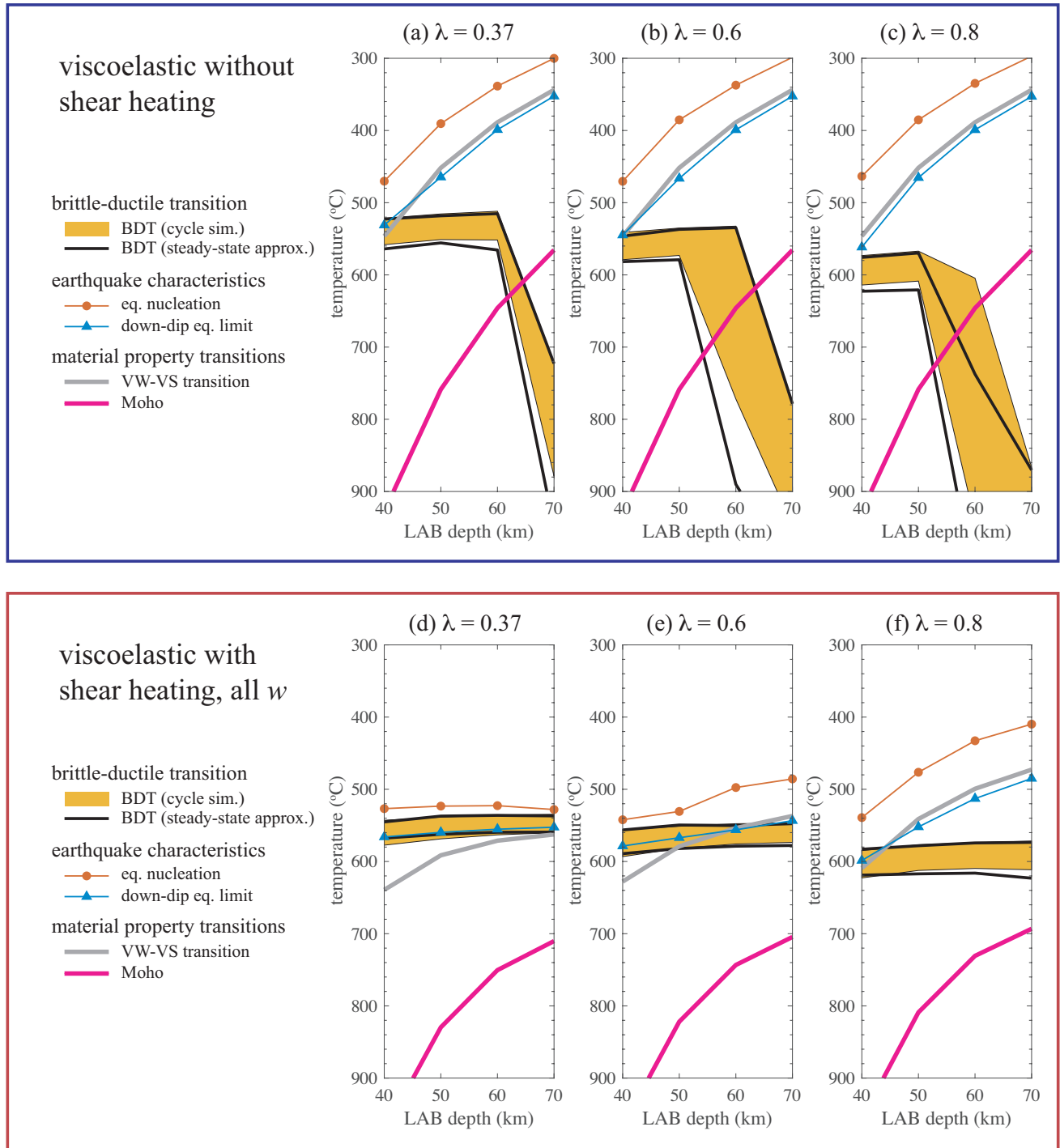


**Figure S4.** Comparison between the temperatures of earthquake nucleation (red circles), the down-dip limit of coseismic slip (blue triangles), and the BDT temperature range (yellow filled regions) for simulations with and without shear heating. For the viscoelastic simulations with shear heating, the average interseismic temperature is used. Also shown are estimates of the BDT temperatures from steady-state results (black lines).

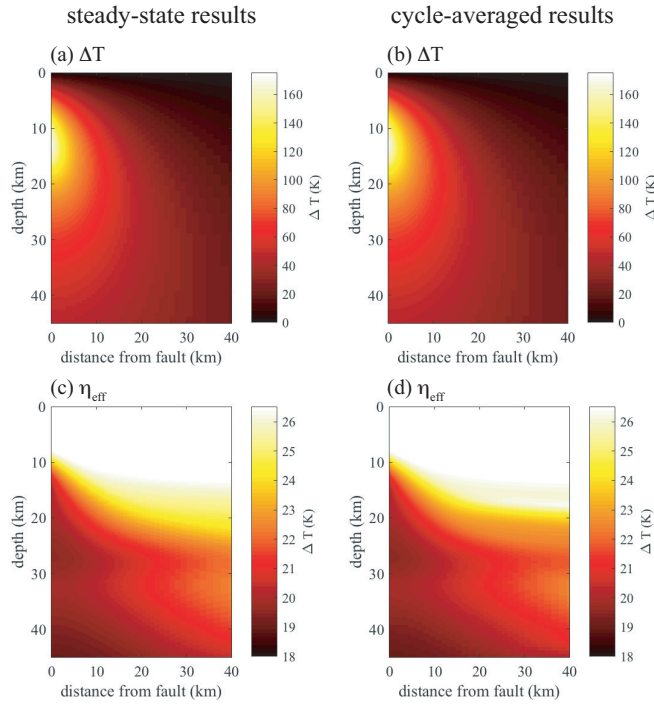


**Figure S5.** Comparison between steady-state and cycle-averaged results: thermal anomaly (a and b), and effective viscosity (c and d). Results are for a 50 km deep LAB and hydrostatic pore pressure.

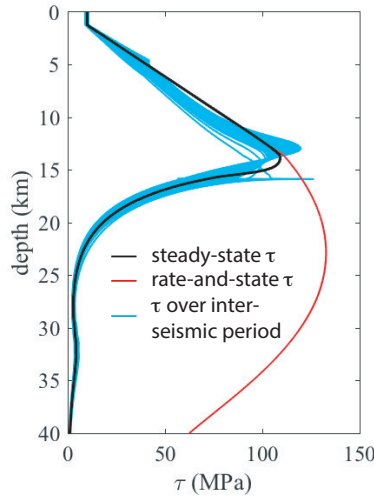


**Figure S6.** The steady-state shear stress on the fault and its deep extension (black) shows good agreement with the interseismic shear stress (blue) for a viscoelastic cycle simulation with shear heating, with a 50 km deep LAB and  $\lambda = 0.37$ . Also shown, for reference, is the shear stress for rate-and-state friction assuming the fault is sliding at the tectonic loading velocity (red).

## References

- 42 Allison, K. L., & Dunham, E. M. (2018). *Earthquake cycle simulations with rate-and-state friction and power-law*  
43 *viscoelasticity* (Vol. 733). doi: 10.1016/j.tecto.2017.10.021
- 44 Ampuero, J.-P., & Rubin, A. M. (2008). Earthquake nucleation on rate and state faults - Aging and slip laws.  
45 *Journal of Geophysical Research*, 113(B1). Retrieved from <http://doi.wiley.com/10.1029/2007JB005082>  
46 doi: 10.1029/2007JB005082
- 47 Dieterich, J. H. (1992). Earthquake nucleation on faults with rate-and state-dependent strength. *Tectonophysics*,  
48 211(1), 115–134. doi: 10.1016/0040-1951(92)90055-B
- 49 Erickson, B. A., & Dunham, E. M. (2014). An efficient numerical method for earthquake cycles in heterogeneous  
50 media: Alternating subbasin and surface-rupturing events on faults crossing a sedimentary basin. *Journal*  
51 *of Geophysical Research: Solid Earth*, 119(4), 3290–3316. Retrieved from [http://doi.wiley.com/10.1002/](http://doi.wiley.com/10.1002/2013JB010614)  
52 [2013JB010614](http://doi.wiley.com/10.1002/2013JB010614) doi: 10.1002/2013JB010614
- 53 Rice, J. R. (1983). Constitutive relations for fault slip and earthquake instabilities. *Pure and Applied Geophysics*  
54 *PAGEOPH*, 121(3), 443–475. doi: 10.1007/BF02590151
- 55 Rice, J. R. (1993). Spatiotemporal complexity of slip on a fault. *Journal of Geophysical Research*, 98(B6),  
56 9885–9907. Retrieved from <http://doi.wiley.com/10.1029/93JB00191> doi: 10.1029/93JB00191
- 57 Rice, J. R., Lapusta, N., & Ranjith, K. (2001). Rate and state dependent friction and the stability of sliding  
58 between elastically deformable solids. *Journal of the Mechanics and Physics of Solids*, 49, 1865–1898. Retrieved  
59 from <http://linkinghub.elsevier.com/retrieve/pii/S0022509601000424> doi: 10.1016/S0022-5096(01)  
60 00042-4
- 61 Ruina, A. (1983). Slip instability and state variable friction laws. *Journal of Geophysical Research: Solid Earth*,  
62 88(B12), 10359–10370. Retrieved from <http://doi.wiley.com/10.1029/JB088iB12p10359> doi: 10.1029/  
63 JB088iB12p10359